

# Evidence for Stream Collision and Disk Formation in Tidal Disruption Events

Hengxiao Guo<sup>1\*†</sup>, Jingbo Sun<sup>1,2</sup>, Shuang-Liang Li<sup>1</sup>, Yan-Fei Jiang<sup>3\*</sup>, Tinggui Wang<sup>4,5</sup>, Defu Bu<sup>1</sup>, Ning Jiang<sup>4,5</sup>, Yanan Wang<sup>7</sup>, Yuhan Yao<sup>8,9</sup>, Rongfeng Shen<sup>10,11</sup>, Minfeng Gu<sup>1</sup>, Mouyuan Sun<sup>12</sup>

<sup>1</sup>Key Laboratory for Research in Galaxies and Cosmology, Shanghai Astronomical Observatory, Chinese Academy of Sciences, 80 Nandan Road, Shanghai 200030, China

<sup>2</sup>University of Chinese Academy of Sciences, 19A Yuquan Road, Beijing 100049, China

<sup>3</sup>Center for Computational Astrophysics, Flatiron Institute, New York, NY 10010, USA

<sup>4</sup>CAS Key Laboratory for Research in Galaxies and Cosmology, Department of Astronomy, University of Science and Technology of China, Hefei, 230026, China

<sup>5</sup>School of Astronomy and Space Sciences, University of Science and Technology of China, Hefei, 230026, China

<sup>7</sup>National Astronomical Observatories, Chinese Academy of Sciences, 20A Datun Road, Beijing 100101, China

<sup>8</sup>Miller Institute for Basic Research in Science, 468 Donner Lab, Berkeley, CA 94720, USA

<sup>9</sup>Department of Astronomy, University of California, Berkeley, CA 94720, USA

<sup>10</sup>School of Physics and Astronomy, Sun Yat-Sen University, Zhuhai, 519082, China

<sup>11</sup>CSST Science Center for the Guangdong-Hongkong-Macau Greater Bay Area, Sun Yat-Sen University, Zhuhai, 519082, China

<sup>12</sup>Department of Astronomy, Xiamen University, Xiamen, Fujian 361005, China

\*To whom correspondence should be addressed; E-mail: hxguo@shao.ac.cn (HXG), yjiang@flatironinstitute.org(YFJ)

**When a star passes through the tidal disruption radius of a massive black hole (BH), it can be torn apart by the tidal force of the BH, known as the Tidal Disruption Event (TDE). Since the UV/optical emitting region inferred**

---

<sup>†</sup>Hengxiao Guo and Jingbo Sun contributed equally to this work

**from the blackbody radius is significantly larger than the circularization radius predicted by the classical TDE theory (1,2), two competing models, stream collision (3) and envelope reprocessing (4,5), were proposed to explain the unexpectedly large UV/optical emitting size. Here, we investigate the variability behaviors (cross-correlation and time delay) of three representative TDEs with continuum reverberation mapping. Our results demonstrate that TDE behavior is clearly inconsistent with the envelope reprocessing scenario. In contrast, the picture of the stream collision, together with the late-time formed accretion disk, can explain heterogeneous observations. This provides compelling evidence that the UV/optical emission originates from stream collisions during the early-stage of TDE evolution and gradually transitions to being dominated by accretion disk with detectable X-ray emission in a late stage. After fading back to a quiescent state, recurrent flares may be observed in some occasions, such as partial TDEs.**

According to the classical theory of Tidal Disruption Event (TDE) (1, 2), a star will be torn apart when it gets into the tidal radius of a massive black hole (BH). Around half of the stellar debris would escape at high speed following a parabolic trajectory while the rest material will fall back to the BH and form an accretion disk (episodes I and III in Figure 4). The circularization of the disk formation could produce a luminous electromagnetic flare and then gradually decline with a power-law (6), regulated by the mass fallback rate. However, with the increased number of optical-selected TDEs discovered by modern time-domain surveys, such as All-Sky Automated Survey for Supernovae (ASASSN) (7) and Zwicky Transient Facility (ZTF) (8), the community found that the observationally inferred UV/optical emitting radius (blackbody radius) is too large compared with the prediction of a circularized debris disk, suggesting that the UV/optical emission of TDE may not be originated from a classical accretion disk (9).

To resolve the tension between observations and theory, two competing models were proposed: the first is the stream collision, which predicts that the trajectory and morphology of the fallback debris stream will be affected by the relativistic effects at pericenter (10), leading to a collision between the subsequent outward stream and previous infalling stream. This collision-induced shock then produces the observed UV/optical flare (3, 11), and the accretion disk forms when the gas falls back to the BH and produces multi-wavelength emission. The second is the envelope reprocessing (5, 12, 13). As the massive BH accretes the fallback gas at a super-Eddington ratio after a fast circularization, the gas will form a radiatively inefficient slim disk (14) with strong outflows. These high-velocity outflows take gas to a larger radius and form a quasi-spherical and optically thick envelope that reprocesses the X-ray/EUV emission from the inner disk to the observed UV/optical emission. Due to the high opacity of the envelope around the accretion disk, the X-ray is thought to be temporarily obscured by ubiquitous outflows during the peak of the UV/optical flare and becomes transparent as the outflow mass rate decreases. While the unexpectedly large UV/optical emitting radius can be explained by both scenarios, the continuum reverberation mapping can provide critical evidence to distinguish the stream collision from the envelope reprocessing. This will yield pivotal insights into the optical and UV radiation origins of TDEs, helping to clarify the overall picture of TDEs and will be foundation for further in-depth investigations. In the following, we study three representative TDEs with excellent data quality for lag analysis to establish a unified picture for TDE evolution.

## **Stream collision dominates the primary UV/optical peak**

TDE AT 2019qiz ( $z = 0.015$ ) was monitored by two independent groups since a very early stage (15, 16), hence sufficient photometric data have been accumulated including a complete UV/optical peak for cross-correlation analyses, as shown in Figure 1. A weak broad  $H\alpha$  compo-

ment persists in the late-time (157 days after the UV/optical peak) optical spectrum, indicative of the possible initial presence of a weak Active Galactic Nucleus (AGN) (15). The peak of the X-ray emission (0.3 – 10 keV) is not detected until  $\sim 30$  days after the UV/optical peak, suggesting the X-ray emission is clearly linked to the TDE, rather than the original weak AGN accretion which usually displays a positive-direction lag for fast-varying component (17–19), namely high-energy band leads low-energy band. In addition, 30-day negative-direction lag is inconsistent with the inverse Compton scattering of NUV seed photons from disk to X-ray in corona in AGN, which predicts a delayed X-ray of at most a few days (20, 21).

Based on the high-cadence multi-band monitoring around the peak, we detect robust positive-direction continuum lags, increasing as a function of wavelength across the UV-optical regime in Figure 1. The inter-band lags of days clearly contradicts the stratified envelope reprocessing scenario (12, 13), which predicts negligible lags between UV and optical bands due to the same scattering light path extending to the outer boundary of the envelope (UV/optical lags in envelope reprocessing). Furthermore, the detected UV lag (UVM2) relative to optical ( $i$ ) is  $2.1_{-0.4}^{+1.1}$  days ( $5.4_{-1.0}^{+2.8} \times 10^{15}$  cm assuming light-speed transmission) with the interpolated cross-correlation function (ICCF, Cross-correlation analysis). The result indicates that the emitting distance between UV and optical has exceeded the blackbody radius ( $R_{\text{bb}} = 6.5 \times 10^{14}$  cm for AT 2019qiz) by a factor of 8.3 at  $4.8\sigma$ . The tension will be further increased if the real separation between UV and optical emitting shells in the envelope is much smaller. Besides, we also detected clear positive-direction lags in UV/optical bands of other ZTF TDEs, revealing a fact that the UV leads the optical emission by a few days in the shock-induced flare is common and their inferred sizes are generally larger than the envelope size ( $\sim 10^{14-15}$  cm) (Lags of ZTF TDEs). Therefore, the observed continuum lags provide determinative evidence against the envelope reprocessing.

An alternative scenario is the stream collision, whose UV/optical flares are caused by the

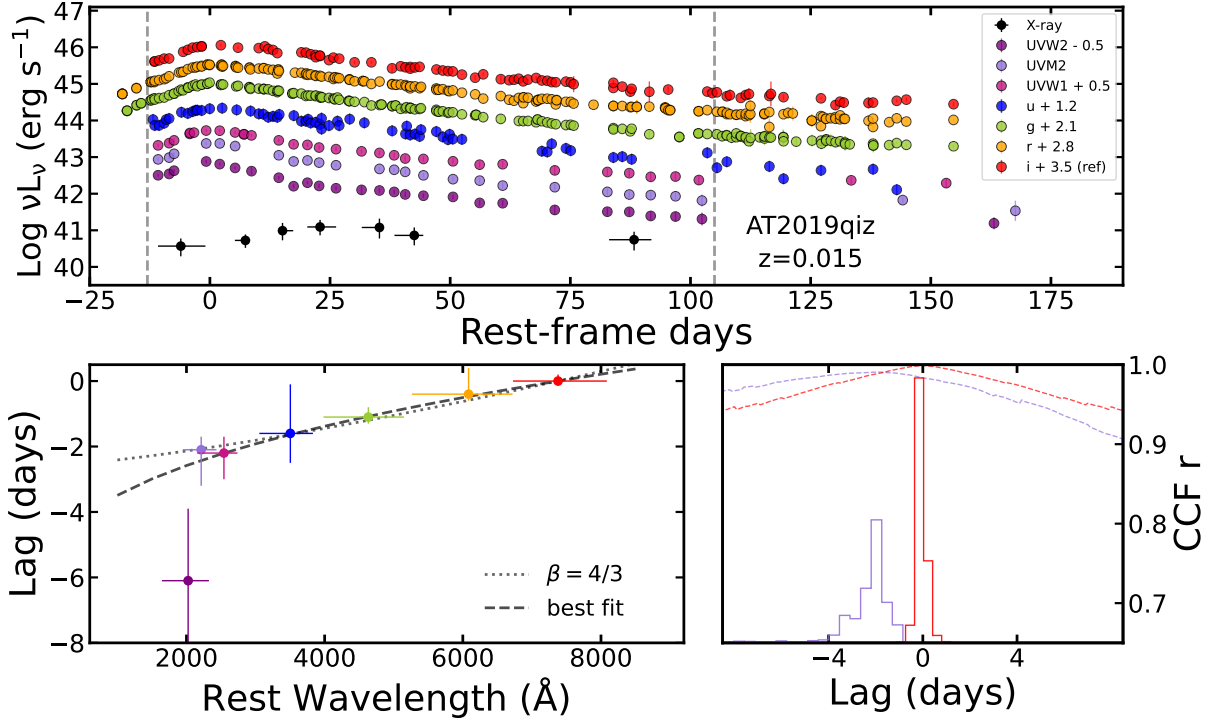


Figure 1: **AT 2019qiz multi-band light curves and ICCF lag measurements.** Upper panel: light curves of UV/optical (host subtracted) and X-ray are obtained from Swift, ZTF, LCO, and Swope observations (15, 16). The combined light curves are listed in Table S1. The photometries used for lag measurements are bracketed by two grey dashed lines and all lags are measured relative to  $i$  band. Bottom left panel: lag increases as a function of wavelength in the rest frame. The black dotted line represents the best power-law fit with a fixed slope of  $4/3$  ( $\chi^2_\nu = 0.43$ ) predicted by the standard thin disk model in AGN. The black dashed line represents the best fit with a free power-law slope ( $\alpha = 0.4$ ,  $\chi^2_\nu = 0.39$ ). Bottom right panel: distributions of lag posteriors and cross-correlation curves for Swift UVM2- $i$  (light purple) and  $i - i$  (red) bands in the rest frame (also see Figure S1 for other bands).

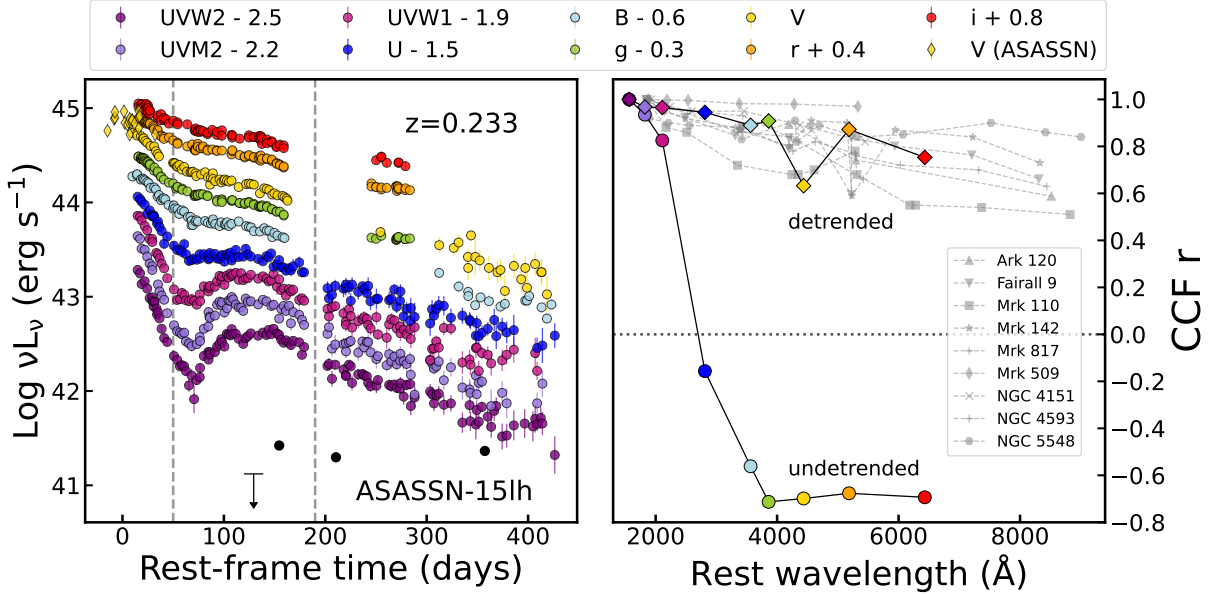


Figure 2: **Host-subtracted light curves of ASASSN-15lh and its inter-band cross correlations compared with local AGNs.** Left panel: multi-band light curves obtained from LCO and Swift observations (26). Black symbols (dot and arrow) represent the soft X-ray (0.5 – 1 keV) luminosity detected by Chandra. Right panel: inter-band cross-correlation coefficient curves (w.r.t. UVW2) of ASASSN-15lh and local AGNs for comparison. The shock component is removed for the detrended version while it is not for undetrended one. The ICCF analysis is based on the period of 50 to 190 days (grey dashed lines), where presents a most significant anti-correlation ( $r_{\text{max}} \sim -0.7$ ) between the UV and optical.

self-interaction of the debris stream. The delay of a few days between UV and optical can be naturally explained by a discrete variant of the stream collision (11, 22), whose successive shock streams produce distinctive orbital velocities. As shown in episode II of Figure 4, a fast inner stream first collides with the infalling stream generating the UV emission, which followed by a slow outer stream producing the optical emission, yielding a lag of a few days between UV and optical. We suggest that these observed lags are unlikely to stem from the diffuse continuum emission observed in AGNs (Diffuse continuum). Additionally, we disfavor their origin from X-ray reprocessing caused by shock-powered outflows (23), considering that the X-ray emission is difficult to be produced in recent simulations (24, 25).

## Disk formation dominates the rebrightening bump

ASASSN-15lh is a luminous transient ( $z = 0.233$ ) discovered by ASASSN. It was initially classified as a superluminous supernova (27), but subsequent evidence suggests it is a TDE originating from a fast-spinning Kerr BH with a mass of  $\sim 10^{8.5} M_{\odot}$  (9, 26, 28). A distinguishing hallmark is the significant rebrightening (RB) bump observed in the UV light curves whereas the optical light curve generally exhibit a power-law decay with a very weak RB trend. Notably, it displays clear short-term AGN-like variability on the RB bump around 100 days after the light peak. The X-ray emission is first detected after the maximum of the RB peak and persists in  $\sim 200$  days, presumably related to disk formation.

Correlation analysis of the UV/optical light curves reveals that the UV and optical light curves around the RB bump ( $\sim 100$  days) are clearly anti-correlated with a maximum ICCF coefficient  $r_{\max} \sim -0.7$  with respect to UVW2 in Figure 2. This is completely inconsistent with the expected strong positive correlation if the UV and optical emissions are driven by the same source (e.g., X-ray/EUV photons) in close reprocessing layers, based on the knowledge of continuum reverberation mapping results in AGNs (18, 29–34). We point out that the opacities of UV and optical emitting shells are expected to be similar in TDE envelope reprocessing model (12), which is difficult to produce completely opposite trends in UV/optical light curves. Therefore, the anti-correlated UV-optical light curves of the RB bump provide another piece of conclusive evidence against the pure reprocessing mechanism during the RB period.

In contrast, if considering a two-component scenario (shock and disk) of the decay light curve, the RB bump can be naturally explained by the disk formation that produces the X-ray/UV/optical emission (35, 36). Whether displaying an RB bump in a certain TDE strongly depends on the relative contributions of the stream collision and disk emission. In our model of disk formation (Disk formation), the unique UV RB bump in ASASSN-15lh is likely caused

by a significant amount of gas falls into the UV/EUV region whose emission peaks near UV regime and its contribution decreases with the increasing wavelength. If we remove the underlying early-stage UV/optical contribution from the stream collision (Figure S7 and Detrending), the multi-band variabilities of the accretion disk recover to positive correlations with coefficients generally decreasing with longer wavelength, similar to the results in AGN continuum reverberation mapping (Inter-band correlations in TDE and AGN), as shown in the right panel of Figure 2. Additionally, the UV-optical lags of the RB bump generally show a positive direction (Figure S7), particularly between UVW1 and  $r$  band with a lag of  $15.0^{+3.8}_{-3.3}$  days ( $4.5\sigma$ ). Note that the phenomenon of the RB bump in UV/optical is not rare in TDEs. We estimate the occurrence rate in a blind ZTF survey  $4/50 = 8\%$  (Figure S10), which is considered as a lower limit since we excluded many TDEs with ambiguous RB bumps (37, 38).

## RB bump and late-time recurring flare

AT 2018fyk ( $z = 0.059$ ) is a both UV/optical and X-ray bright TDE, first discovered by ASASSN (39–41). Similar to ASASSN-15lh, it exhibits a clear RB plateau in UV/optical, accompanied with high-cadence X-ray monitoring, although the peak of the UV/optical flare is not captured. The UV and X-ray follow-up lasts over 1300 days from a high accretion state to a quiescent state in Figure 3, allowing us to explore the correlations of X-ray/UV/optical in different stages of this TDE.

In stage A, the first detection of X-ray is in a low state but rises rapidly within 6 days, and then its variability pattern correlated with UV/optical for a period over  $\sim 60$  days. Later on, the UV/optical resumes to decline, whereas the X-ray gets further brightened showing an opposite variability trend between 100 – 300 days after the peak, probably due to the state transition (41). Similar to ASASSN-15oi (42), the optical spectra in the RB plateau (at  $\sim 45$  days) show clear low-ionization Fe II emission lines, indicative of optically thick and high-density gas, again



providing compelling evidence of the formation of an optically thick accretion disk during the RB bump (39). In stage B, both UV and X-ray present AGN-like variations with an almost flat trend rather than a TDE-like power-law decline, and eventually followed by a dramatic drop occurring in both UV and X-ray by several orders of magnitudes, indicating a sudden exhaustion of accretion flow in the disk after a timescale of  $\sim 500$  days. The presence of low-ionization Fe II emission lines ( $\sim 45$  days), and a flat decay pattern accompanied with AGN-like variability ( $\sim 200 - 400$  days) serve as corroborative evidence for the disk formation during/after the RB bump.

We measured the lags between X-ray and UV in AT2018fyk with  $9.2_{-6.0}^{+6.1}$  days at stage A (X-ray leads the UV,  $r_{\max} = 0.57$ ), and  $4.0_{-1.4}^{+1.4}$  days at stage B (UV leads the X-ray,  $r_{\max} = 0.55$ ) (also see Figure S8 and S9). The opposite lag directions may demonstrate different physics and manners of the gas supplement (gas fallback or accretion flow) in different stages (Disk formation).

In stage C, the UV and X-ray emission remarkably recover to the level of stage B ( $\sim 10\% L_{\text{UV,peak}}$ ). The recurrent flare contributes significantly to comprehending the entire long-term evolution of TDEs. Given the comparable X-ray and UV luminosities (43), such recurring event indicates a new supplement of the accreting gas, probably after a secondary stream collision in a partial TDE or sporadic accretion resulting from secondary outflow interactions (23). Similar behavior has been reported in other TDEs, such as AT 2020vdq (44), as depicted in Figure S17 (Recurring flare).

## A unified picture of TDE evolution

Based on three representative TDEs, we illustrate a general evolutionary picture of TDEs, namely the stream collision and disk formation scenario, assuming that all TDEs follow a similar physical process. As depicted in Figure 4, a star is first disrupted by the tidal force of

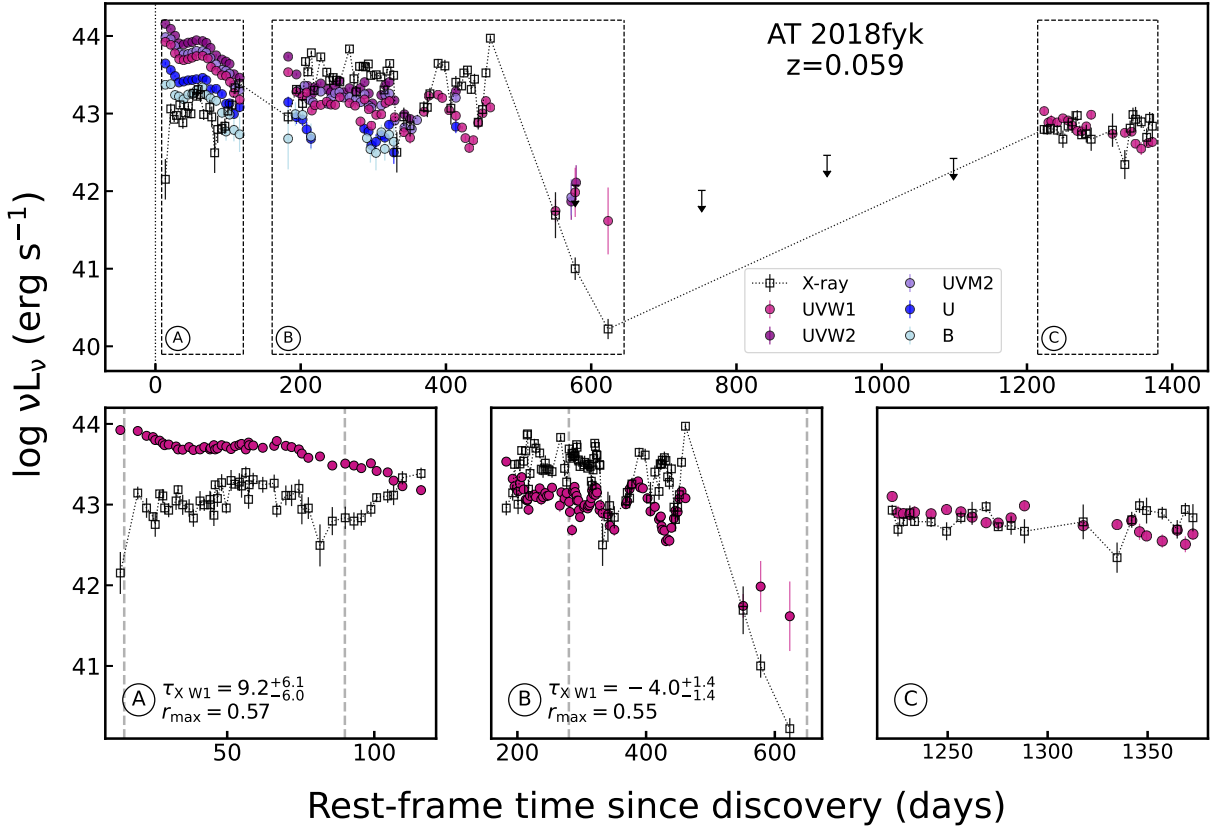


Figure 3: **The long-term evolution of AT 2018fyk in UV/optical and X-ray.** Light curves are obtained from Ref (43). Dots represent different host-subtracted UV/optical light curves and squares/arrows stand for the X-ray data including the upper limit. All the light curves are binned every 5 days for demonstration. Three periods in the upper panel are zoomed in showing in lower panels and in Figure S8 & S9, and ICCF results are listed in each panel. Note that the UV and X-ray are clearly anti-correlated between  $\sim 100$  to 300 days, which are not considered for lag measurements.

the massive BH at the pericenter in episode I. The properties of the outward stream debris are regulated by relativistic effects (10), and the first primary UV/optical peak of the TDE flare is caused by the stream collision at a few hundreds of gravitational radius (Collision point). Due to the disparity in velocities in a discrete stream collision picture in episode II (11, 22), the UV emission usually rise first followed by the optical emission with a lag of days. Meanwhile, an optically thick and anisotropic envelop will be produced after the stream collision, accompanied with strong outflows (45, 46).

The gas energy dissipates/accumulates and angular momentum is redistributed during the stream collision in episode II. The gas may directly plunge into the massive BH on a freefall timescale or circularize (Timescales) until forming a complete accretion disk. The UV/optical emission on the RB bump is a composition of the shock emission (shock collision and envelope emission) and the radiation from the newly formed accretion disk. Whether showing an obvious UV/optical RB bump strongly depends on the relative contributions between shock and disk emission in episode III. The shock emission usually dominates the early-stage emission of the TDEs and fades away with a power-law decay, thus highlighting the late-time disk emission with occasional AGN-like variability lasting for a viscous timescale. The late-time accretion is also confirmed by the long-standing FUV emission (47) and X-ray detection (48). The delayed formation of the accretion disk naturally explains the delayed X-ray emission relative to the shock-induced UV/optical flare, and the two-component radiation mode also accounts for the heterogeneous correlations among X-ray/UV/optical (see also Power spectral density). However, if a star is not fully disrupted, such as a partial TDE scenario in episode IV&V, we will record a recurring flare with a long-term monitoring (43, 44). This intermittent ignition also alleviates the long-standing missing energy problem in TDEs (49).

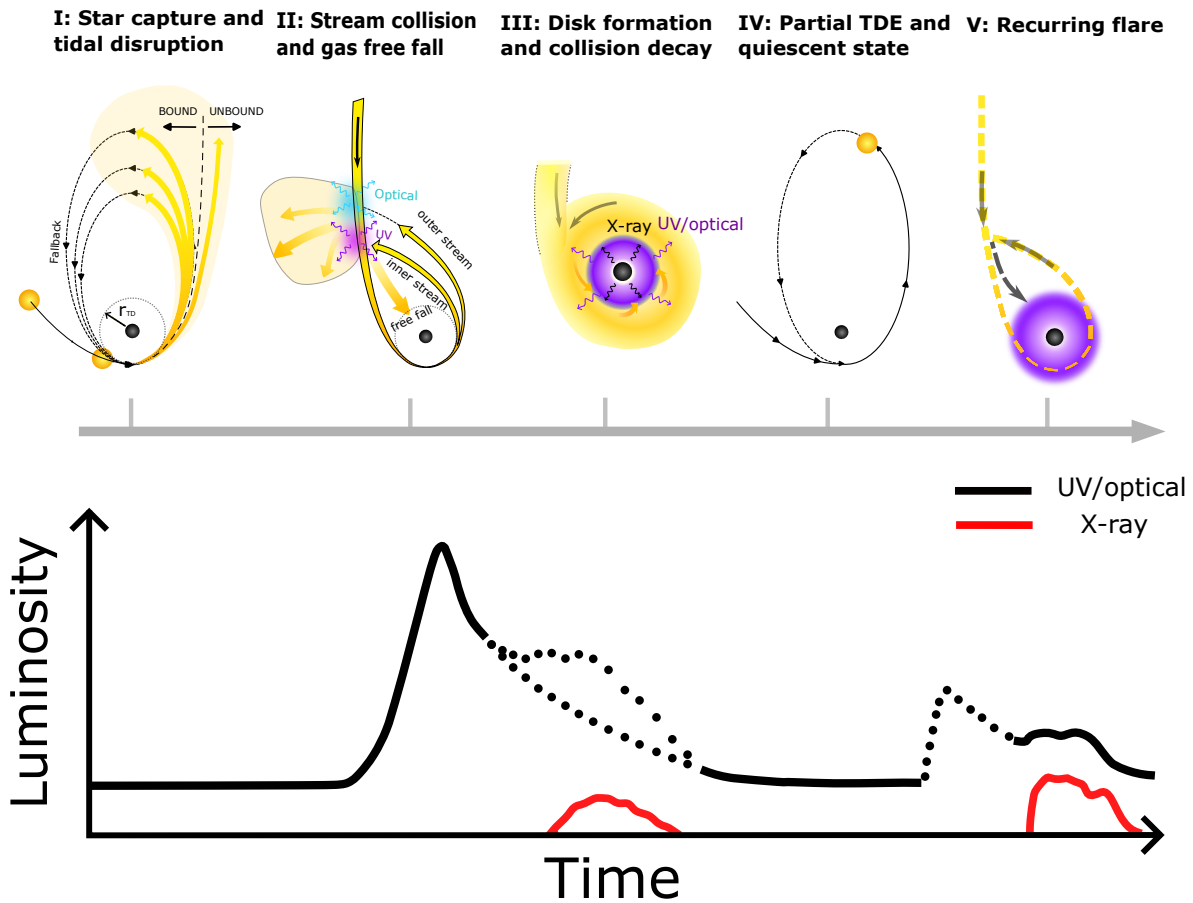


Figure 4: A schematic of TDE evolution in stream collision and disk formation scenario, and corresponding light curves. Upper panels: Episode I: a star is torn apart at the pericenter and around half of the stellar debris escapes while the rest material falls back to the BH. Episode II: because of the relativistic effects at pericenter, stream-stream collision occurs at a few hundreds of gravitational radius producing the primary UV/optical flare, an optically thick envelope, and strong outflows. The differential velocities of the discrete successive streams result in the observed continuum lags in UV/optical. Episode III: gas falls back to the BH and forms the new accretion disk emitting X-ray emission, accompanied with strong outflows. The stream collision gradually decays in this period. If the disk component is significant relative to the shock emission, we may observe the X-ray emission and the RB bump in UV/optical light curves. Episode IV: the BH becomes quiescent again after all gases on the disk are accreted onto the BH. If the star is not fully disrupted and still bounded by the BH, it will fall back again into the tidal-disruption radius as a partial TDE. Episode V: the BH will be re-ignited as in episode II and III, and a recurring flare will be observed, accompanied with X-ray emission. Bottom panel: corresponding light curves in X-ray/UV/optical. The dotted line indicates an alternative evolution path in episode III or an unobserved period between episode IV and V. Note that X-ray may not be detected due to the limited sensitivity of telescopes.

## Materials and Methods

### Cross-correlation analysis

To measure the continuum lag, we adopt the most commonly used technique, interpolated cross-correlation function (ICCF) (50) with the Python package `PYCCF` (51). It simply determines the lag at which the correlation between the two light curves is maximized, independent of any assumptions about whether the two light curves are related to each other.

All the light curves are moved to the rest frame time and transformed to the luminosity regime assuming a  $\Lambda$ CDM cosmology, with  $H_0 = 72.0$ , and  $\Omega_m = 0.3$ . Note that all the UV and optical light curves are host-subtracted. The lag search range is usually set to  $\pm 30$  days in the rest frame (except for some longer X-ray delays) and search the lags with a 0.1-day grid spacing. The correlation coefficient ( $r_{\max}$ ) describes the strength and direction of the correlation. ICCF utilizes the traditional flux randomization/random subset sampling (FR/RSS) procedure (50, 52) to obtain the lags and uncertainties. This Monte Carlo method randomizes the flux measurements by their uncertainties (FR) and randomly chooses a subset of light-curve points (RSS) to build the peak/centroid lag distribution, whose median value and  $1\sigma$  range serve as the peak/centroid lag and error, respectively. We carried out 10000 FR/RSS iterations for each measurement. The centroid lags are generally adopted. For sanity check, we also confirmed that all centroid lags are broadly consistent with peak lags (also see Figure S2). To best demonstrate the inter-band lags, we usually select the bluest or reddest band as a reference band depending on the data quality. We have checked that changing a reference band do not alter our results.

### Lags of ZTF TDEs

To confirm the positive-direction continuum lags of TDEs between UV and optical, we also collected the multi-band light curves of 30 TDEs discovered in ZTF survey (37). We excluded 12 objects with incomplete coverage of the UV/optical flare peak due to seasonal gaps, since

the flare is the primary variable feature used to determine the lag. This criterion allowed us to focus on the most informative cases. Our final sample consists of 18 objects with available *gr*-band light curves, alone with additional 6 objects with *i*-band light curves and 3 objects with UV data (see Table S2).

As illustrated in Figure S2, most of the inter-band lags are positive yet the uncertainties are large, subjecting to the cadence and noise issues. Totally, 7 lags (3 *gr* and 4 *gi* lags) are significantly deviated from zero at  $> 1\sigma$  confidence level and three representative examples having *gri* light curves are displayed in Figure S3. More importantly, we also discovered two additional TDEs in Figure S4 showing robust positive UV/optical lags increasing as a function of wavelength as AT 2019qiz, yielding a lag detection rate of 100% between UV and optical bands given the ZTF cadence, albeit with a small sample size. The detected UV (UVW2) lags relative to optical (*r*) of AT 2019azh and AT 2020zso are  $10.8_{-3.8}^{+8.0}$  days and  $7.6_{-1.9}^{+1.3}$  days ( $c\tau = 2.8_{-1.0}^{+2.1} \times 10^{16}$  cm and  $2.0_{-0.5}^{+0.3} \times 10^{16}$  cm), exceeding their blackbody radii  $R_{\text{bb}} = 5.6 \times 10^{14}$  and  $8.9 \times 10^{14}$  (37) by factors of 50 at  $2.7\sigma$  and 22 at  $3.8\sigma$ , respectively. This is clearly indicative of a common occurrence of high-energy leading low-energy bands in the shock-induced peak.

Furthermore, we compared the blackbody radius ( $R_{\text{bb}}$ ) with the inferred size of the UV/optical emitting distance ( $c\tau$  assuming light-speed transmission in reprocessing) for 13 sources showing positive lags. We remind that according to the envelope reprocessing picture, the emitting separation across UV to optical should be much smaller than the whole envelope size,  $c\tau \ll R_{\text{bb}}$ . Figure S5 reveals that the size inferred by  $c\tau$  are generally larger than the complete envelope size ( $R_{\text{bb}}$ ). If we naively assume UV/optical emitting separation is around  $0.1R_{\text{bb}}$ , values of  $c\tau$  in all targets are much larger than  $0.1R_{\text{bb}}$ , albeit with large uncertainties. This finding further confirms that envelope-like structure is difficult to produce such a long lag between UV and optical emissions.

## UV/optical lags in envelope reprocessing

Previous work (12) proposed an extended, quasi-spherical, optically thick envelope, with a stratified structure where the effective photosphere for high-energy emissions (e.g., soft X-ray continuum emission) is located deeper within the envelope compared to the effective photosphere for low-energy emissions (e.g., UV/optical continuum emission). The effective photospheres ( $\tau_{\text{eff}} \sim \sqrt{\tau_{\text{es}}\tau_{\text{abs}}} = 1$ ) at different wavelengths represent layers beyond which most photons can escape the envelope without being re-absorbed through electron scattering, as illustrated in Figure S6. According to the reprocessing model, both the UV and optical emissions are driven by soft X-ray emission from the accretion disk and subsequently reprocessed by different layers of the envelope, with a negligible reprocessing timescale. To ensure the consistency with real observations, we assume that the envelope is sufficiently thick to absorb all soft X-ray photons and convert them into UV/optical emission. The time delay of UV/optical relative to X-ray variability strongly depends on the diffusion time (or electron scattering opacity,  $\tau_{\text{es}}$ ) through the envelope, namely the travel time between UV and optical photospheres to the outmost envelop boundary, i.e.,  $t_{\text{UV}} = (L1 \times \tau_{\text{L1,UV,es}} + L2 \times \tau_{\text{L2,UV,es}})/c$  and  $t_{\text{opt}} = (L1 \times \tau_{\text{X-ray,L1,es}} + L2 \times \tau_{\text{opt,L2,es}})/c$ , respectively.  $L1$  and  $L2$  represent the separations between different shells in Figure S6. While electron scattering opacity is determined by the scattering material, independent of the emission wavelength (53), i.e.,  $\tau_{\text{L1,UV,es}} = \tau_{\text{L1,X-ray,es}}$  and  $\tau_{\text{L2,UV,es}} = \tau_{\text{L2,opt,es}}$ . Therefore, no theoretical time delay between UV and optical is expected through the path of  $L1 + L2$  in this simple scenario. This is apparently at odd with the results of TDE continuum reverberation mapping, thus disfavoring the envelope reprocessing model.

In addition, it is possible that when the envelope size and effective photosphere temperature change with time, the peak of blackbody emission will also shift. Typically, when the luminosity and effective temperature decrease with time, the spectrum peak can move from the UV

band to the optically band, which can also cause a delay between UV and optical lightcurve. However, this mechanism will also cause significant evolution of spectrum slope with time. When the blackbody emission peaks at the UV band, we expect the total energy emitted in the UV band is larger than the total energy emitted in the optical band. When the peak moves to the optical band, the ratio should reverse. The real system can be more complicated if the effective temperature at the photosphere is not uniform. But the fact that the ratio between luminosity in UV and optical bands of TDE lightcurves shows very small variations with time suggests that this is also unlikely the explanation.

### **Diffuse continuum**

Continuum reverberation mapping of AGN has demonstrated that AGN continuum variations exhibit wavelength-dependent and positive-direction lags that scale as  $\tau \propto \lambda^{4/3}$ , which is consistent with the prediction of the standard thin disk model (54). These inter-band continuum lags are expected within the framework of the X-ray reprocessing model, wherein high-energy photons emitted from the corona above the disk center are absorbed and reprocessed to lower energies at larger radii in the disk. By measuring these lags, which correspond to the light-travel time across the disk, continuum reverberation can yield valuable insights to determine the sizes of AGN accretion disks. However, current AGN continuum reverberation mapping campaigns have revealed that the inferred disk sizes, based on the lags, are several times larger than the predictions of the standard disk model (19). Robust evidence of the lag excess around Balmer jump at 3647 Å (or  $u/U$  band lag excess) relative to the scaling relation ( $\tau \propto \lambda^{4/3}$ ) indicates the unexpected large continuum lags mainly attribute to the diffuse continuum originating from the inner broad-line region (31). The mechanism of the diffuse continuum covering from  $\sim 1000 - 10000$  Å is dominated by free-free, free-bound, and scattered continuum emission of Hydrogen and Helium and excited by X-ray/EUV photons (18, 19, 55).



We compared positive-direction continuum lags in three TDE (AT 2019qiz in Figure 1, AT 2019azh and AT 2020zso in Figure S4) with that in AGNs, and concluded that the continuum lags in TDE are unlikely caused by diffuse continuum for three reasons: Firstly, lack of the source emitting high-energy photons (e.g., X-ray/EUV photons) makes it unlikely to be excited and contribute significantly to the first light peak before the formation of the disk. Note that since the lag of a few days are common in normal TDEs residing in quiescent galaxies, we suggest the pre-exist weak AGN in AT 2019qiz has negligible contribution to the observed continuum lags. Secondly, there is no clear  $u/U$ -band lag excesses around  $3647 \text{ \AA}$  in the rest frame, as commonly seen in most AGNs. Finally, the best-fit power-law slopes observed in our TDEs is much smaller than that from the standard disk or including the diffuse continuum. Therefore, we suggest that the positive-direction continuum lags of the stream collision peak in TDEs are unlikely caused by the diffuse continuum as AGNs.

## **Inter-band correlations in TDE and AGN**

To compare the continuum correlations of the disk emission between the RB bump of ASASSN-15lh and normal AGNs, we collect 9 well-studied local AGNs with the most extensive monitoring: Akn 120 (29), Fairall 9 (30), Mrk 110 (32), Mrk 142 (34), Mrk 817 (33), Mrk 509 (56), NGC 4151 (34), NGC 4593 (31), NGC 5548 (18). The multi-band photometric cadences of these continuum reverberation campaigns are around 1 day with a baseline of 3 to 6 months. A key result of these campaigns is that the UV and optical light curves are very tightly correlated (the correlation between X-ray and UV/optical is relatively weak) and the inter-band lags increase as a function of wavelength as expected by the X-ray reprocessing. Their cross-correlation coefficients estimated using the standard ICCF method with respect to the Swift UVW2 band are exhibited in the right panel of Figure 2. It is clear that the shock-contribution-subtracted coefficient curve ( $r_{\text{max}}$  as function of wavelength) follows a general decay trend of

those in AGNs, supporting a disk origin of the RB bump in ASASSN-15lh.

## Detrending

According to our TDE evolution picture illustrated in Figure 4, the observed UV/optical light curve is a superposition of emissions from the shock and accretion disk, each governed by distinct mechanisms. To accurately measure the inter-band lags, it is necessary to perform the detrending (57) to separate the shock and disk components and avoid mutual interference in lag measurements, particularly when their flux contributions are comparable. It is not applicable to X-ray light curves as they are supposed to be purely originated from the accretion disk. Also, detrending is not performed for TDEs with a single flare, where the UV/optical emission is predominantly governed by stream collisions.

In this work, we define the RB bump as a feature showing significant flux excess relative to the decay trend during the fading stage, rather than at the end of the decay, which may be mimicked by late-time AGN variability (e.g., AT 2018fyk in stage B) or photometric residuals after subtracting the host component. For TDEs exhibiting an RB bump as shown in Figure S10 and Table S3, we employed either a power-law or an exponential detrending in  $t - \nu L_\nu$  space for light curves in each band following previous studies (58). Specifically, we first attempt to fit the light curve with a power-law function:

$$L_\nu = L_{\nu, \text{peak}} \left( \frac{t - t_{\text{peak}} + t_0}{t_0} \right)^p, \quad t_{\text{turnover}} > t > t_{\text{peak}} \quad (1)$$

where  $t$  is the rest frame time,  $t_{\text{peak}}$  is the light peak time,  $t_{\text{turnover}}$  is the time of the first turnover point of the concave light curve, and  $t_0$  is the power-law normalization.  $L_{\nu, \text{peak}}$  is the peak luminosity at frequency  $\nu$ . We simply focus on the decay regime ( $t > t_{\text{peak}}$ ) since our aim is to remove the shock contribution. The power-law function is a widely used model for describing the decay phase of TDE and generally provides good fits for most cases. However, a few ZTF

TDEs still exhibit obvious deviations from the power-law modeling (38). Then, an exponential function is also used to fit all the light curves for comparison:

$$L_\nu = L_{\nu, \text{peak}} e^{-\frac{t-t_{\text{peak}}}{\tau_{\text{decay}}}}, \quad t_{\text{turnover}} > t > t_{\text{peak}} \quad (2)$$

where  $\tau_{\text{decay}}$  is the decay time.

We adopt a maximum likelihood approach to estimate the posterior distributions of our model parameters given the light curves and priors listed in Table S4. To efficiently draw samples from the posterior probability distributions of the model parameters, we use `emcee` (59), a python implementation of the affine invariant ensemble sampler for Markov Chain Monte Carlo (MCMC). Similar to previous works (38, 58), uncertainties of the light curves are amplified by a factor  $f$  according to its intrinsic scatter in each target to complement the potentially underestimated photometric error. We use 100 walkers and 5000 steps, discarding the first 1500 steps to ensure convergence. Then we adopt the model with the best  $\chi_\nu^2$  as our fiducial result as listed in Table S5. Note that we also examined the lag measurements with different detrending methods, and confirmed that the lag results are generally comparable within uncertainties.

## Lags of RB bumps

To investigate the details of the disk formation, we focus on seven TDEs with RB bumps shown in Figure S10. Multi-band light curves are not sufficient in AT 2021uqv and AT 2020acka for lag measurements. In addition, no significant non-zero lags of the RB bump can be detected between  $g$  and  $r$  bands in AT 2019baf, albeit with high-cadence ZTF light curves. Fortunately, significant lag information is extracted from AT 2020ocn and AT 2019avd.

AT 2020ocn is a spectroscopically confirmed TDE at  $z = 0.07$  discovered by ZTF (37). The optical monitoring of this event unveils a relatively weak yet discernible RB bump occurring approximately 60 days subsequent to the primary peak. We consider it as a robust RB bump since a corresponding UV peak is observed, which should not be a delayed flare to the first

peak due to the widely observed positive-direction lags in the shock-driven peak, although the first peak is not covered by the UV data. No significant lags among UV/optical bands are detected due to the weak variability. Nevertheless, the luminous X-ray emission is detected by Swift/XRT at 0.3 – 2 keV, showing a clear delay ( $\sim 50$  days) relative to the RB bump in UV/optical. We suggest this is a piece of strong evidence of the outside-in variability transition within the accretion flows on the nascent accretion disk (Disk formation).

AT 2019avd was initially classified as a TDE candidate at  $z = 0.028$  (60) and subsequently proposed to be a genuine TDE (61, 62) upon revealing a significantly broad RB bump and multi-band properties in Figure S12. Other distinctive TDE features, such as the He II emission line, Bowen fluorescence lines, and high-ionization coronal lines observed during the RB bump, provide strong evidence of the disk formation. We suggest that, most importantly, the significant negative-direction lag of  $-46.9_{-16.5}^{+10.5}$  days ( $4.5\sigma$ ) with  $r_{\max} = 0.66$  between X-ray and optical bands further validates its TDE nature, rather than AGNs. Note that the UV/optical turnover around 700 days is not related to the missing peak of X-ray around 580 days, see the Swift light curve in Figure 2 of (62). This again demonstrates the outside-in variability transition picture as AT 2020ocn. In addition, mild positive-direction lags are also detected in UV/optical:  $\tau_{W1,r} = 19.3_{-17.1}^{+13.8}$  and  $\tau_{gr} = 4.8_{-3.3}^{+2.9}$  days.

## Collision point

The expected photosphere temperature of the shocked gas from stream-stream collision is correlated with the distance  $r_{\text{shock}}$  to the BH where the collision happens. Assuming the stream is in a parabolic orbit, the velocity before the shock is  $v_s = (2GM_{\text{BH}}/r_{\text{shock}})^{1/2}$ . Thickness of the stream  $H_s$  is typically determined by the balance between the pressure gradient inside the stream and the tidal force from the BH as  $H_s \approx 2r_{\text{shock}} \sqrt{r_{\text{shock}} c_s^2 / (2r_g c^2)}$  (45), where  $c_s$  is the sound speed of the stream and  $r_g$  is the gravitational radius of the BH. Notice that for

a typical sound speed of 10 km/s, thickness of the stream is smaller than  $1\%r_g$ . Then typical density of the stream can be estimated as  $\rho_s = \dot{M}/(H_s^2 v_s)$ , where  $\dot{M}$  is the mass flux carried by the stream. The shock due to stream-stream collision converts the kinetic energy to the thermal energy. The temperature of the downstream gas  $T_d$  can be estimated by energy conservation  $\rho_s v_s^2/2 = 3\rho_d k_B T_d/(2\mu m_p) + a_r T_d^4$ , where  $k_B$  and  $a_r$  are Boltzmann's constant and radiation constant respectively,  $\rho_d$  is the downstream gas density and we account for both gas internal energy and radiation energy density. The downstream gas will expand and cool and the photosphere temperature will be smaller than  $T_d$  by a factor of 20 or more depending on the  $\dot{M}$  (45). Since wavelengths of UV and optical bands correspond to typical temperature of  $2 \times 10^4$  and  $10^4$  K, this requires the collision point to be smaller than  $10^3 r_g$  for  $10^6 M_\odot$  BH and a few hundreds  $r_g$  for  $10^8$  solar mass BH. Otherwise the collision will not be able to produce hot enough gas for the prompt emission. Since the stream-stream collision point is likely the place where the disk starts to form, the estimated value of  $r_{\text{shock}}$  should set the outer edge of the disk.

## Power spectral density

Based on our scheme presented in Figure 4, the first and second peaks in UV/optical TDE are produced by different mechanisms, leading us to anticipate distinct PSDs that elucidate how the power of the variability signal is distributed across various frequencies. We collected all the TDEs from the ZTF TDE sample (37) and in Figure S10 showing RB bumps. We require light curves with relatively good sampling and coverage, which leaves us 14 objects exhibiting complete shock peaks and 6 targets covering RB bumps. In addition, to purely focus on the shock and disk emission, we further purify the light curves by removing the non-flare/non-RB bump segments that may bias the PSD slope at the low-frequency end. Then, we convert the unevenly sampled light curves to PSDs via the widely used Lomb–Scargle periodogram (63). The normalized PSD is fitted by a power-law ( $\text{PSD} \propto \nu^\alpha$ ) after eliminating the measurement

noise ( $2\delta t\sigma^2$ , where  $\delta t$  and  $\sigma^2$  are the average time spacing and measurement noise variance, respectively). Uncertainties are estimated via the Monte Carlo method. Figure S13 presents the examples of the PSD fitting. Our analysis reveals that the PSD slope originating from disk emissions maintains a relatively uniform shape around  $\alpha = -2$  across timescales ranging from days to months, consistent with AGNs (64–66). In contrast, the PSD slope for shock emissions exhibits a broader distribution, spanning from  $-3.0$  to  $-0.5$ , consistent with the expectation of shock emission due to the diverse physical conditions in individual shocks. Our results of PSD thus further support the shock collisions and disk formation scenario, albeit with a small sample size and heterogeneous observations (e.g., seasonal gaps and cadence). In addition, the PSD slopes of RB bumps in UV/optical/X-ray light curves in comparable qualities are similar, e.g., AT 2018fyk, akin to in AGNs (67), suggesting a common disk origin for multi-band emissions.

## Timescales

According to the shock-disk model of TDEs, several important timescales can be identified:

The angular momentum of the gas has redistributed during the stream-stream collision. In an extreme scenario where all the angular momentum is dissipated, the gas undergoes freefall and is ultimately accreted by the BH during the episode II illustrated in Figure 4. If the gas fall back from the apocenter, the freefall timescale ( $t_{\text{ff}}$ ) can be given by (26)

$$t_{\text{ff}} \sim \left(\frac{2R_a}{g}\right)^{1/2} = 2.64 \times 10^{-2} \left(\frac{1+e}{1-e}\right)^{3/2} \beta^{-3/2} r_* m_*^{-1/3} \text{ (day)}, \quad (3)$$

where  $R_a = (1+e)R_p/(1-e)$  is the radius of apocenter,  $R_p$  and  $e$  are the pericenter radius and the eccentricity, respectively. The penetration factor is given by  $\beta = R_t/R_p$ , where  $R_t = R_*(M_{\text{BH}}/M_*)^{1/3}$  is the tidal radius.  $r_* = R_*/R_\odot$  and  $m_* = M_*/M_\odot$  are the star radius and mass scaled with the Sun, respectively. If the collision point is much below the apocenter (23),  $t_{\text{ff}}$  serves as an upper limit,  $t_{\text{ff,max}}$ .

Conversely, the fallback timescale, denoted as  $t_{\text{fb}}$ , describes the time it takes for the bound gas to fall back to the pericenter of the BH without losing any angular momentum during episode I of Figure 4. A maximum estimation for this timescale (9) is given by:

$$t_{\text{fb,max}} \approx 40(M_{\text{BH},6})^{1/2} m_*^{-1} r_*^{3/2} \text{ (day)}, \quad (4)$$

where  $M_{\text{BH},6} = M_{\text{BH}}/10^6 M_\odot$ .

The circularization timescale, denoted as  $t_{\text{cir}}$ , signifies the duration required for accreting material to transition from an elliptical orbit to a circular orbit. It can be approximated as (9):

$$t_{\text{cir,max}} \approx 3.32 \times 10^2 (M_{\text{BH},6})^{-7/6} \beta^{-3} m_*^{-1} r_*^{3/2} \text{ (day)}. \quad (5)$$

The viscous timescale, denoted as  $t_{\text{vis}}$ , corresponds to the time required for the BH to accrete all the gas present in the accretion disk at the outer disk radius, corresponding to the viscous processes in episode III and IV in Figure 4. It can be approximated as (26):

$$\begin{aligned} t'_{\text{vis,max}} &\approx \left( \frac{8R_p^3}{GM_{\text{BH}}} \right)^{1/2} \left[ \frac{H_{2R_p}}{2R_p} \right]^{-2} \alpha^{-1} \\ &= 5.27 \times 10^{-1} \beta^{-3/2} m_*^{-1/2} r_*^{3/2} \frac{0.1}{\alpha} \left[ \frac{2R_p}{H_{2R_p}} \right]^2 \text{ (day)}, \end{aligned} \quad (6)$$

where  $H_{2R_p}$  is the disk scale-height at  $2R_p$  assuming  $R_{\text{out}} = 2R_p$  (68) and  $\alpha$  is the Shakura-Sunyaev parameter of disk (54). However, the real disk size is related to different parameters, e.g., the collision point and the redistributed gas angular momentum, which can be much larger than  $2R_p$  (23), such as a factor of 10 or  $\sim 200 R_g$  at EUV emitting zone for a BH mass of  $10^6 M_\odot$  (e.g., the inner purple disk in Figure S16, Disk formation), then it roughly corresponds to  $t_{\text{vis,max}} \sim 10t'_{\text{vis,max}}$ .

Therefore, the maximal time delay between the stream collision and the RB peak or RB timescale can be given as:

$$t_{\text{RB,max}} = t_{\text{fb,max}} + t_{\text{cir,max}} + t_{\text{vis,max}}. \quad (7)$$

Since  $t_{\text{ff}}$  and  $t_{\text{RB,max}}$  correspond with the lower and upper limit of time delay, respectively, the real one should be  $t_{\text{ff}} \lesssim t_{\text{RB}} \lesssim t_{\text{RB,max}}$ .

According to detailed studies of stream-stream collisions in TDEs (23, 45, 69), the fate of gas after the stream collision in episode II of Figure 4 can be broadly classified into three categories: freefall gas, accreting gas, and unbound gas, primarily determined by the carried angular momentum. The freefall gas, which has completely transferred its angular momentum, directly plunges into the BH following the freefall timescale ( $< t_{\text{ff,max}}$ ). While the gas with reduced angular momentum undergoes a gradual inward spiral along elliptical orbits, eventually returning to the vicinity of the BH within the fallback timescale ( $t_{\text{fb}} \lesssim t_{\text{fb,max}}$ ), although a small amount of gas may gain angular momentum to circularize at larger radius to produce optical emission. During this process, the gas transitions from an elliptical orbit to a circular orbit within a circularization timescale ( $t_{\text{cir}} \lesssim t_{\text{cir,max}}$ ), and simultaneously/subsequently form an accretion disk on a viscous timescale ( $t_{\text{vis}} \lesssim t_{\text{vis,max}}$ ). In the case of unbound gas, the majority of it escapes the gravitational confinement of the BH. However, a small fraction of the unbound gas may undergo secondary stream collisions (23, 45) and subsequently falls back towards the BH. The typical timescale is very uncertain, depending on the collision point, carried angular momentum, etc.

As shown in Figure S10, the lower limit of RB timescale is roughly 2.2 days assuming the collision point is near apocenter, where  $e = 0.9$  and  $\beta = r_* = m_* = 1$  are adopted. The maximal time delay roughly varies from 700 to 1000 days for the BH with mass  $10^6 M_\odot < M_{\text{BH}} < 10^{8.5} M_\odot$ , where  $\alpha = 0.1$ ,  $2R_p/H_{2R_p} = 10$ , and  $R_{\text{out}} = 20R_p$  are adopted. It is found that all the observed time delay of TDE in Table S3 are well located between  $t_{\text{ff}}$  and  $t_{\text{RB,max}}$ , indicating the RB timescales in TDEs are generally consistent with the shock collision and disk formation picture. Note that the real maximum viscous timescale is very sensitive to the disk scale-height.



## Disk formation

To investigate the process of disk formation, we have compiled the currently available TDEs exhibiting a significant RB bump in Figure S10, and listed the corresponding inter-band lags (Lags of RB bumps), if available, in Table S6. Our observations reveal several key findings:

- The rising time of the RB bump exhibits a wide distribution, spanning from a few tens of days to several years.
- The observations suggest a bidirectional propagation of variability signals, with UV radiation slightly leading optical but potentially significantly leading X-ray emissions.
- The observed UV-X-ray lags are significantly longer than those observed in AGN reprocessing, yet with an opposite direction.
- A lag direction switch is noticed in AT 2018fyk, where a positive lag direction between X-ray and UV emissions is observed during the RB stage, while it transitions to a negative direction during the later accretion phase.

It is clear the lags we observed here are from different physical origins compared with the lags between variabilities of different continuum emission bands found for many AGNs (70). The lags are also significantly shorter compared with the viscous timescales predicted by the standard thin disk model if X-ray, UV and optical photons are produced by such a disk. In fact, even for normal AGNs, the thin disk model is far from successful to explain many observational properties of the accretion disks when the accretion rate is a few percent of the Eddington value (71, 72). When the stream collides with itself in TDEs, the shock will not only convert the kinetic energy to the thermal energy, but also produce a broad distribution of angular momentum with respect to the black hole for the downstream gas (23, 45, 46). The gas that is still bound to the black hole will fall back and circularize at different radii according to the angular momentum

they have. The gas that gains angular momentum during the collision will circularize at larger radii and emit radiation at a longer wavelength, while the gas that loses angular momentum during the process will circularize at smaller radii and emit radiation at a shorter wavelength, as shown in Figure S16. Therefore, we propose a model of a small disk emitting UV to X-ray emission plus an optical ring outside.

The delayed X-ray is caused by the gradually spiral-in accretion flow from the EUV/UV emitting region (a few hundreds of  $R_g$ ) on an inflow timescale. During this processing, magnetic field may also play an important role in the formed accretion disk to reduce the inflow time compared with the estimated timescale based on the viscosity as used in the thin disk model. When the star is disrupted, stellar magnetic field will get stretched and be carried by the stream (73, 74), which can be the seed magnetic field that gets amplified due to differential rotation when the disk is formed. If the seed magnetic field is in a favorable configuration (for example, with a poloidal component), strong toroidal magnetic field can be generated and elevate the accretion disk (75–77). This type of accretion disk has a larger disk scale height compared with the standard thin disk model for the same accretion rate and therefore the inflow timescale is significantly reduced. Numerical simulations of isolated black hole accretion disks have confirmed the existence of this type of accretion flow (69, 78, 79).

On the other hand, we observed robust UV-optical lags on RB bump (e.g., ASASSN-15lh). This requires an extra optical emitting ring outside the disk since the small disk truncated at UV/EUV emitting radius cannot directly produce the observed UV-optical lags and luminosities. This ring is produced by the gas gained angular momentum after the stream-stream collision or outflow gas. We emphasize that it represents a most effectively emitting ring, rather than totally isolated from the inner disk as the gas angular momentum is continuously distributed. The tight correlation between UV and optical could be due to the same gas origin from the collision point, e.g., similar mass distribution or intrinsic temperature fluctuation during the

collision. The lag between UV and optical may correspond to the time it takes for the gas to circularize at different radii.

For a Schwarzschild BH with a mass of  $\sim 10^6 M_\odot$ , the size of the accretion disk is relatively large in unit of  $R_g$ . The fallback gas after circularization will first generate the EUV emissions and then gradually spiral inward on a reduced inflow timescale, producing the soft X-rays (0.2 keV) with  $T_{\text{peak}}$  reaching up to  $4 \times 10^5$  K for a Schwarzschild BH ( $T_{\text{peak}} \approx 4 \times 10^5 \dot{m}^{1/4} (0.1/\eta)^{1/4} M_{\text{BH},6}^{-1/4}$ ,  $\dot{m} = 1$ ,  $\eta = 0.1$ ). Note that the gas fallback location is not necessary to be the emitting peak of the spectral energy distribution (SED). The observed negative-direction delay between X-ray and optical emission in AT2019avd and AT2020ocn indicate the location of fallback gas is close to the UV emitting annulus, rather than directly plunging into the X-ray emitting region. For the BH with a relatively larger mass, e.g., AT 2018fyk ( $M_{\text{BH}} = 10^{7.7} M_\odot$ ), the disk size will be much smaller. The positive-direction lag between X-ray and UV may indicate the returning gases first fallback into the inner X-ray emitting region, then fill the EUV/UV zone or spread outwards on a diffuse timescale (80). While the late-time negative-direction lag indicates a spiral-in accretion flow after the fallback gas becomes negligible, which is similar to the slow variable component seen in AGNs (21). For even larger BH masses ( $\geq 10^8 M_\odot$ ), the TDE could only occur in fast spinning BHs whose tidal radius is very close to the gravitational radius. This results in the formation of a very small accretion disk (68). In addition, given a BH mass of  $10^{8.5} M_\odot$ , the peak temperature ( $T_{\text{peak}}$ ) of the accretion disk is approximately  $9.5 \times 10^4$  K, corresponding to the EUV band (at  $\sim 300$  Å). This explains why the UV RB bump in ASASSN-15lh is much more prominent than that in optical. The commonly observed positive-direction lags in UV/optical likely infer the late formation of the optical emitting ring outside due to the longer circularization timescale. The undetected UV/optical lags in AT 2020ocn and AT 2018fyk could be attributed to either the low quality of the light curves or the absence of an intrinsic optical emitting region.

## Recurring flare

Except for AT 2018fyk, other TDEs have demonstrated recurring flares, such as AT 2020vdq (81). It is discovered by ZTF in a quiescent galaxy and classified as a TDE based on its first flare. The first flare does not show any clear RB bumps. Remarkably, an unambiguous recurring flare, with even an higher luminosity, is observed a few hundreds of days after the first flare, as shown in Figure S17. Based on the follow-up observations, they suggest that the second flare in AT 2020vdq is caused by a partial TDE considering multi-band properties (X-ray and radio detection) and spectral features. In addition, the recurring flare also show a positive-direction lag in UV/optical, similar to that of the shock peak (Lin et al. in prep.). Combined with AT 2018fyk, we speculate that the recurring flare produced by a partial TDE may be very common, although we cannot rule out the possibility of late-time direct accretion of fallback gas originated from secondary stream-stream collisions. Current observations do not provide unambiguous evidence to pin down the underlying mechanism, whether it involves partial TDEs, recurrent accretion, or other scenarios. High-cadence deep X-ray monitoring is a key to reveal the intrinsic physics.

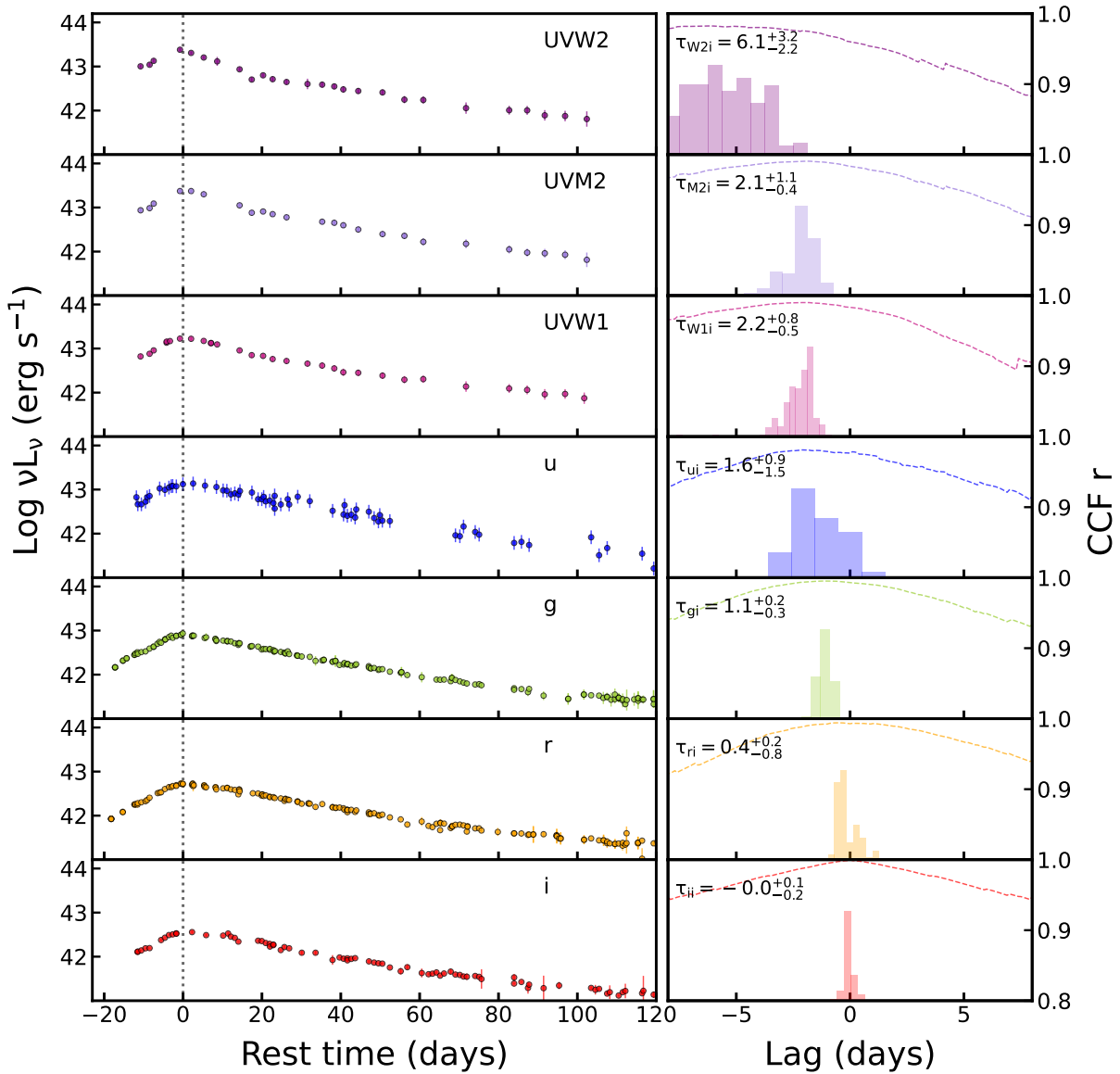


Figure S1: **Multi-band light curves of AT2019qiz and ICCF lag measurements.** Left panel: multi-band light curves are observed by the Neil Gehrels Swift Observatory. Light curves are ordered by wavelength, from the shortest (top) to longest (bottom) wavelength. The *i* band light curve is selected as the reference band. Its peak ( $t = 0$ ) is marked by a black dotted line. Right panel: ICCF lag posteriors based on Monte Carlo method with FR/RSS. The median values of these posteriors serve as the peak lags and their uncertainties are estimated from the  $1\sigma$  range of the distributions. The CCF curves (dashed lines) are shown in each panel. All their peak values ( $r_{\max}$ ) are close to 1, indicating the strong correlations among these multi-band light curves.

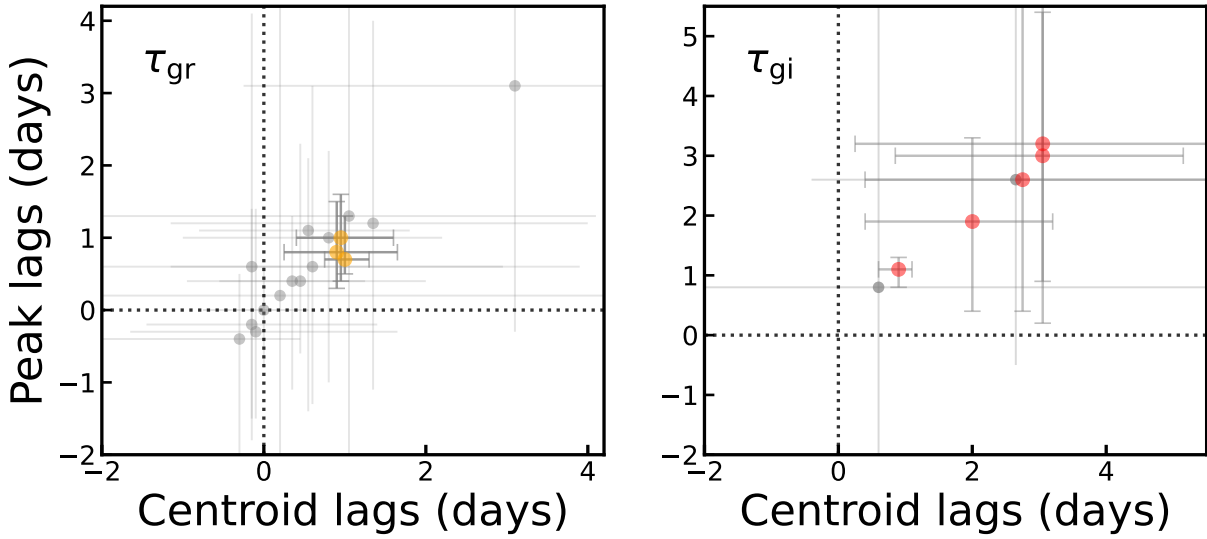


Figure S2: **Continuum lags for ZTF TDEs.** Both centroid and peak lags measured with the ICCF method are exhibited, basically consistent with each other.  $\tau_{gi}$  are generally larger and more significant than the  $\tau_{gr}$  lags as expected. Three  $\tau_{gr}$  (orange dots) and four  $\tau_{gi}$  (red dots) are larger than zero at  $> 1\sigma$  level. Grey dots represent the lags consistent with zero in errors.

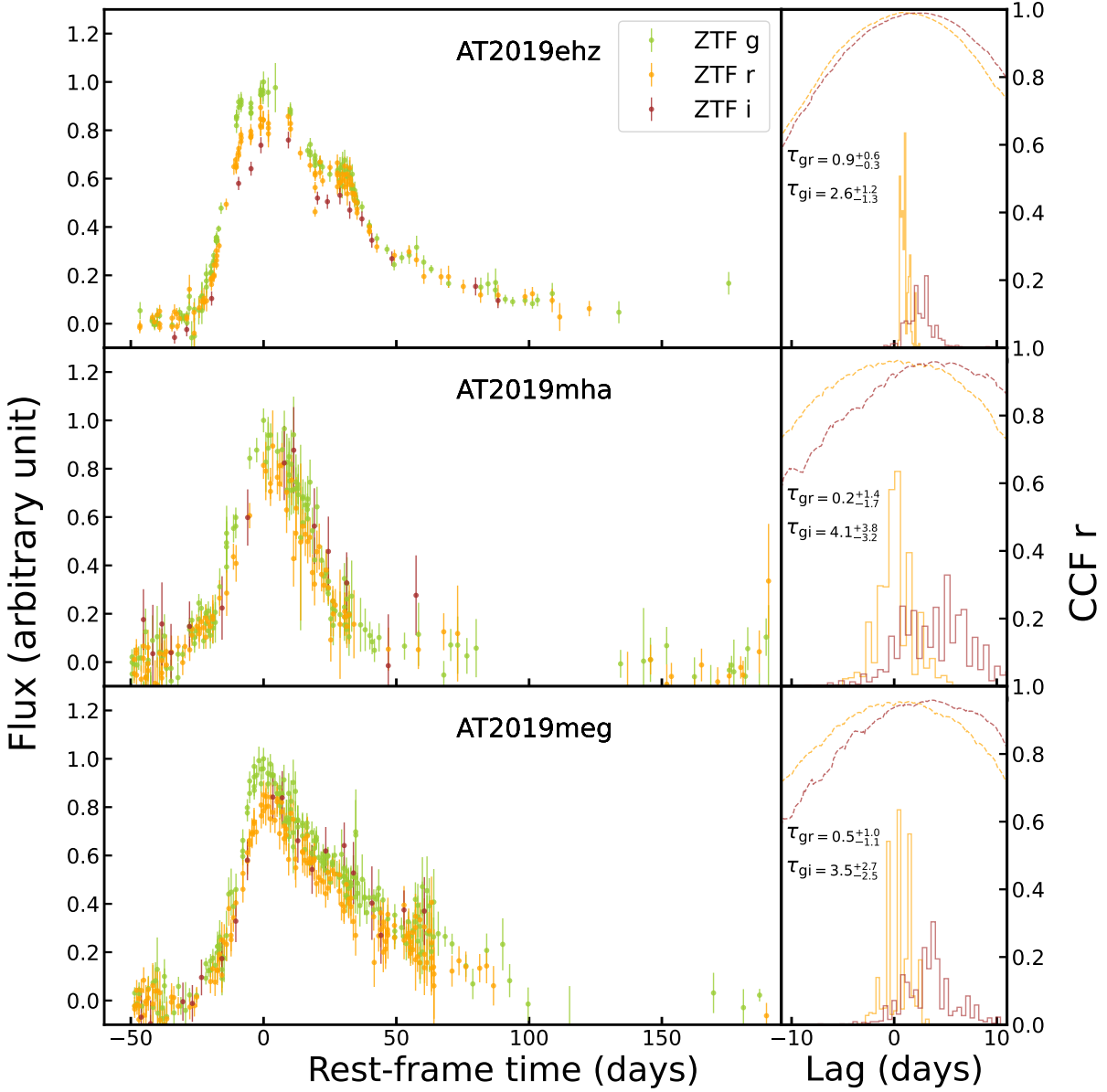


Figure S3: **Three examples of ZTF TDE light curves with clear positive-direction lags.** All the light curves are host subtracted. It is clear that the flare peaks of the longer wavelengths are delayed relative to the  $g$  band maximum light, although the  $i$ -band cadence is much lower than that of  $gr$  bands. As expected,  $gi$  lags are longer than the  $gr$  lags.

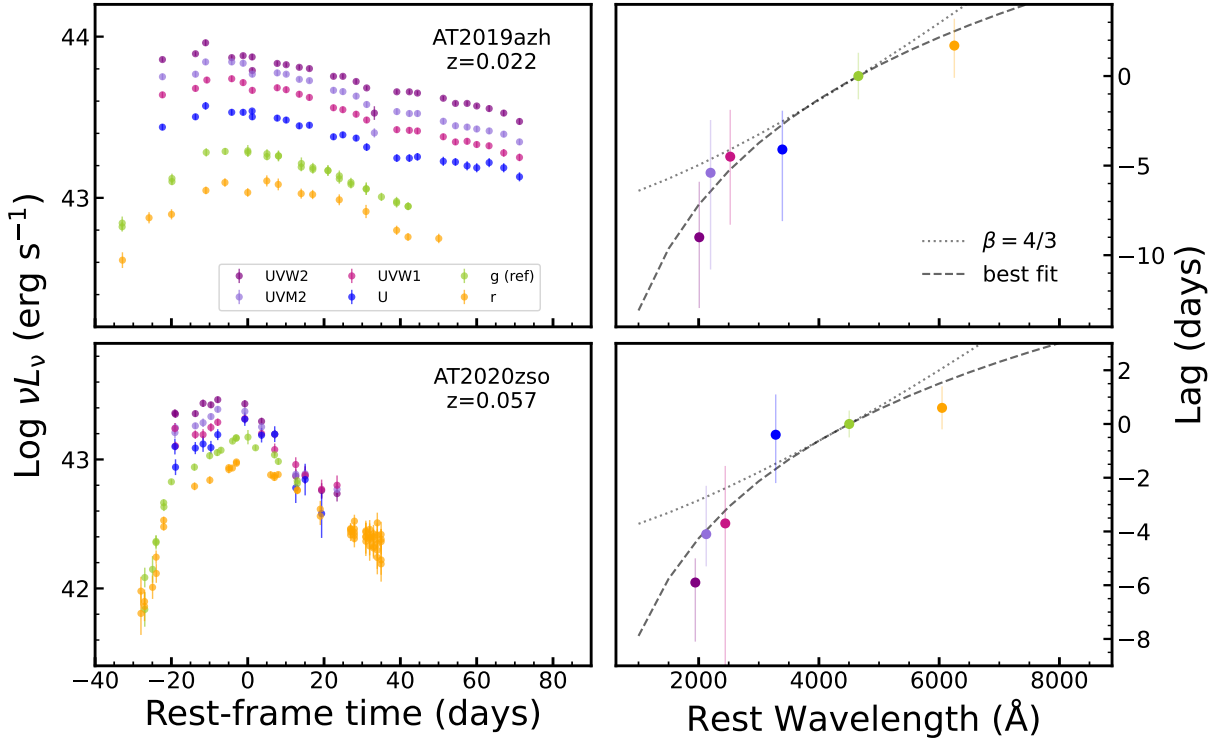


Figure S4: **Multi-band TDE light curves and continuum lags in AT 2019azh and AT 2020zso.** Both objects show a few days of positive-direction continuum lags across the UV-optical band. The lags are measured relative to the  $g$ -band light curve. The lag model predicted by the standard thin disk theory (black dotted line) is clearly inconsistent with the observed lags, indicating the lag is not caused by the diffuse continuum. The dashed line is the best power-law fit.



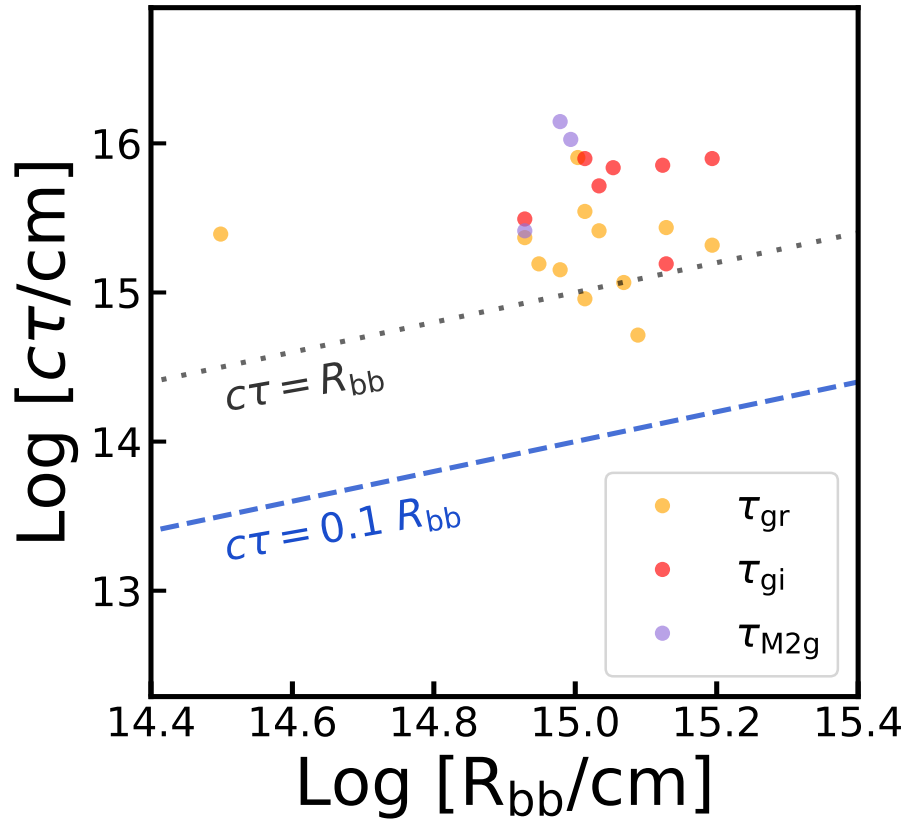


Figure S5: **Blackbody radius vs. continuum lag inferred distance.** The total sample comprises 13 sources, with 12 in *gr*, 7 in *gi*, and 3 in UV bands. The dotted grey and dashed blue lines respectively show  $c\tau = R_{bb}$ ,  $0.1R_{bb}$  assuming a light speed propagation.

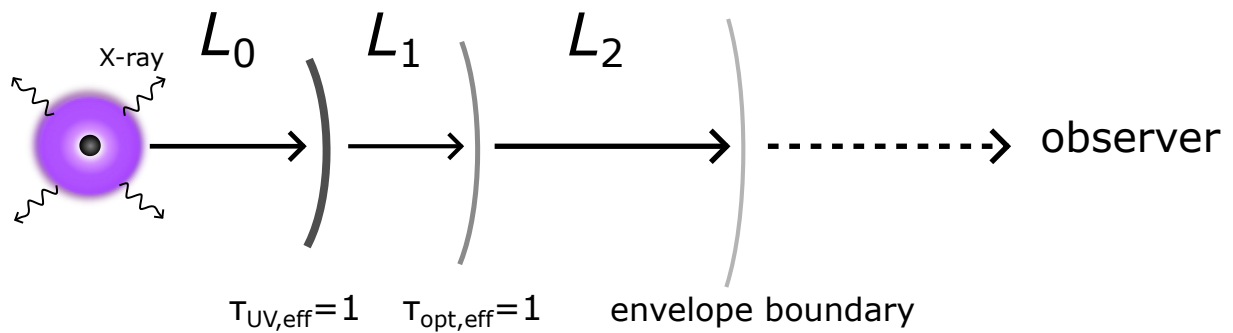


Figure S6: A **simplified scheme of stratified TDE reprocessing model from ref (12)**. The accretion disk emitting soft X-ray is encapsulated by the quasi-spherical gas. Different layers represents the effective photospheres of UV, optical and electron scattering (envelope boundary). The effective photospheres at different bands refer to the boundaries beyond where most photons will electron scatter their way out of the envelope without being re-absorbed.

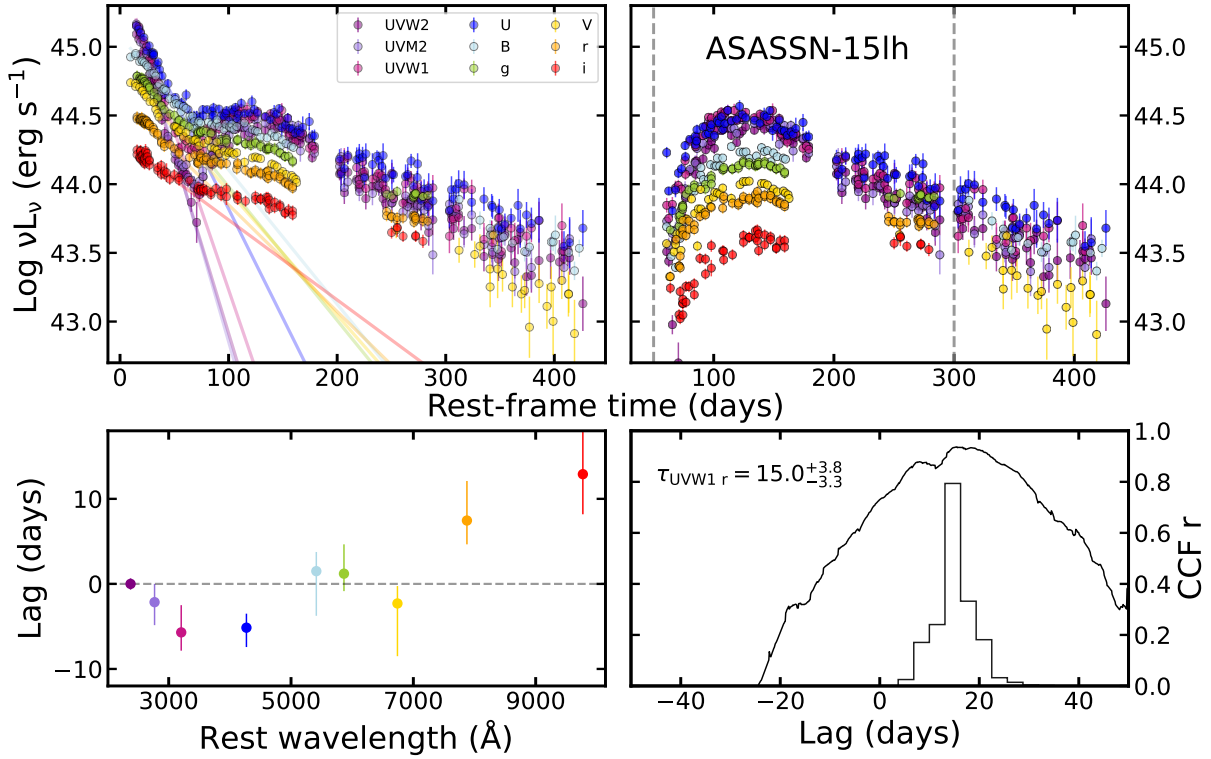


Figure S7: **An example of light-curve detrending to separate the RB bump in ASASSN-15lh.** Upper panels: multi-band light curves before and after an exponential detrending. The region between two grey dashed lines is utilized for lag measurements. Bottom left panel: inter-band lags as a function of wavelength. Bottom right panel: lag posterior and CCF curve between UVW1 and  $r$  band.

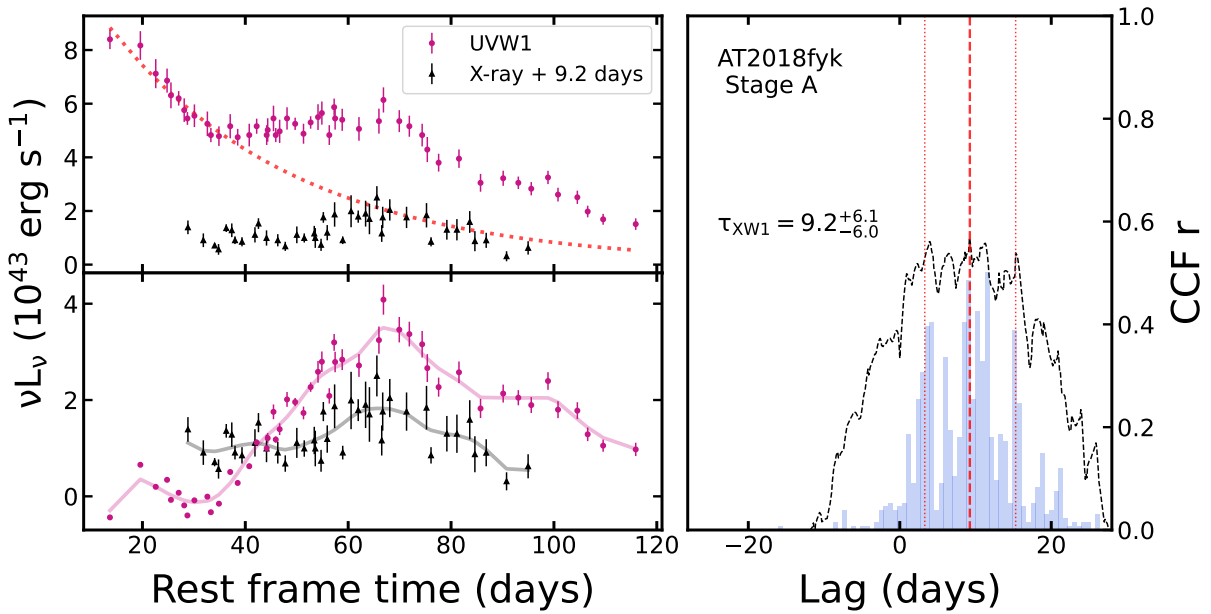


Figure S8: **Lag measurements of AT 2018fyk in stage A.** Left panels: the exponential de-trending (red dotted line) applied to the UVW1 light curve to remove the shock contribution. The X-ray light curve is aligned with the measured lags of 9.2 days with ICCF. The selected light-curve segment may represent relatively pure mechanism and show the most significant CCF results. Right panel: lag posterior (blue histogram) and CCF curve (black dashed line). Red dashed and dotted lines denote the median value and  $1\sigma$  error, respectively.

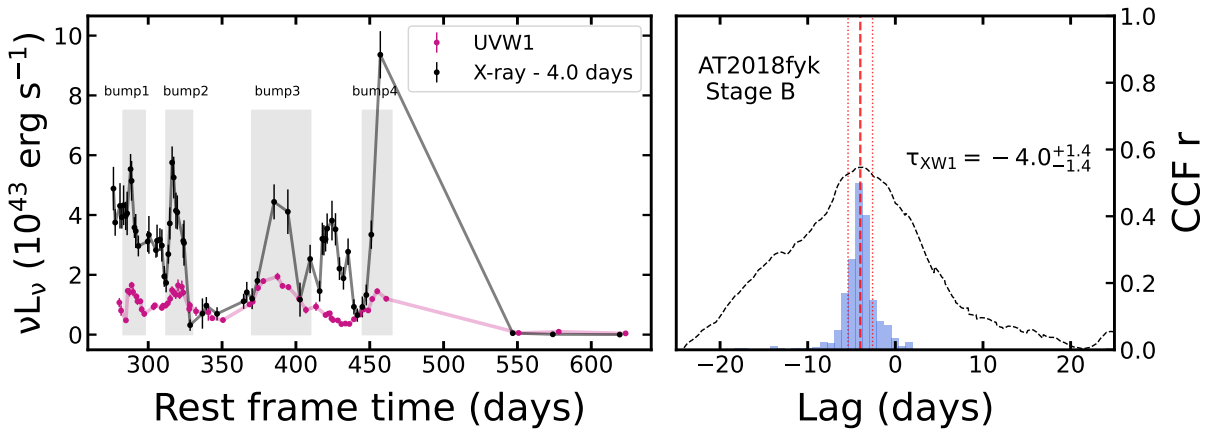


Figure S9: **Lag measurements of AT 2018fyk in stage B.** Left panel: aligned UV and X-ray light curves. The X-ray light curve is shifted with the ICCF lag of  $-4$  days. Shaded regions represent the corresponding bumps in two light curves. The selected light-curve segment may represent relatively pure mechanism and show the most significant CCF results. Right panel: lag posterior (blue histogram) and CCF curve (black dashed line). Red dashed and dotted lines denote the median value and  $1\sigma$  error, respectively.

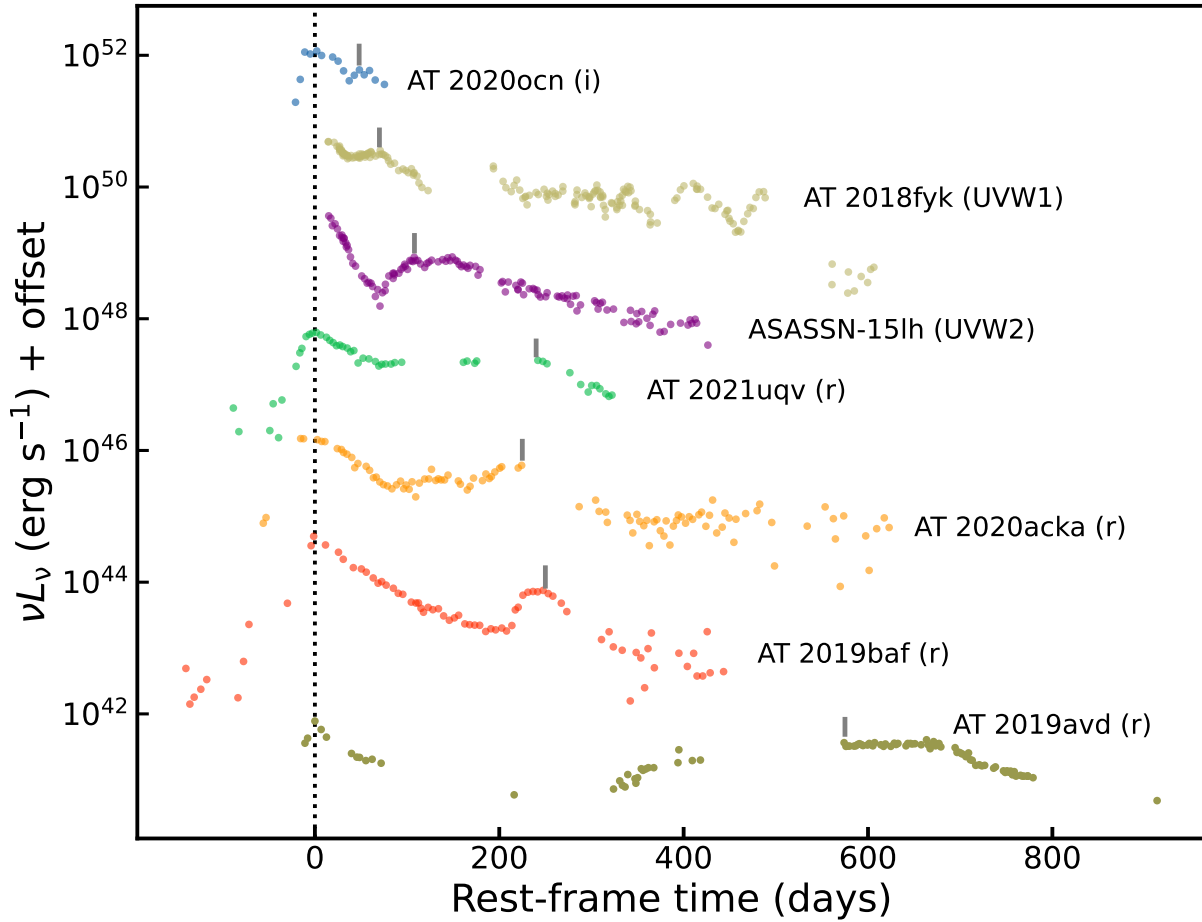


Figure S10: **TDEs exhibiting prominent RB bumps reported in the literature.** Target names and corresponding bands are listed for each TDE. The first peak and the RB peak of the light curve are indicated by grey lines. Note that peak time of ASASSN-15lh was known by ASASSN V band in Figure 2, and  $t = 0$  for AT 2018fyk represents the timing of its discovery, expected to be very close to the peak. AT 2019baf, AT 2020ocn, AT 2020acka, and AT 2021uqv are from a ZTF sample of 50 TDEs (37, 38), yielding an occurrence of 8%.

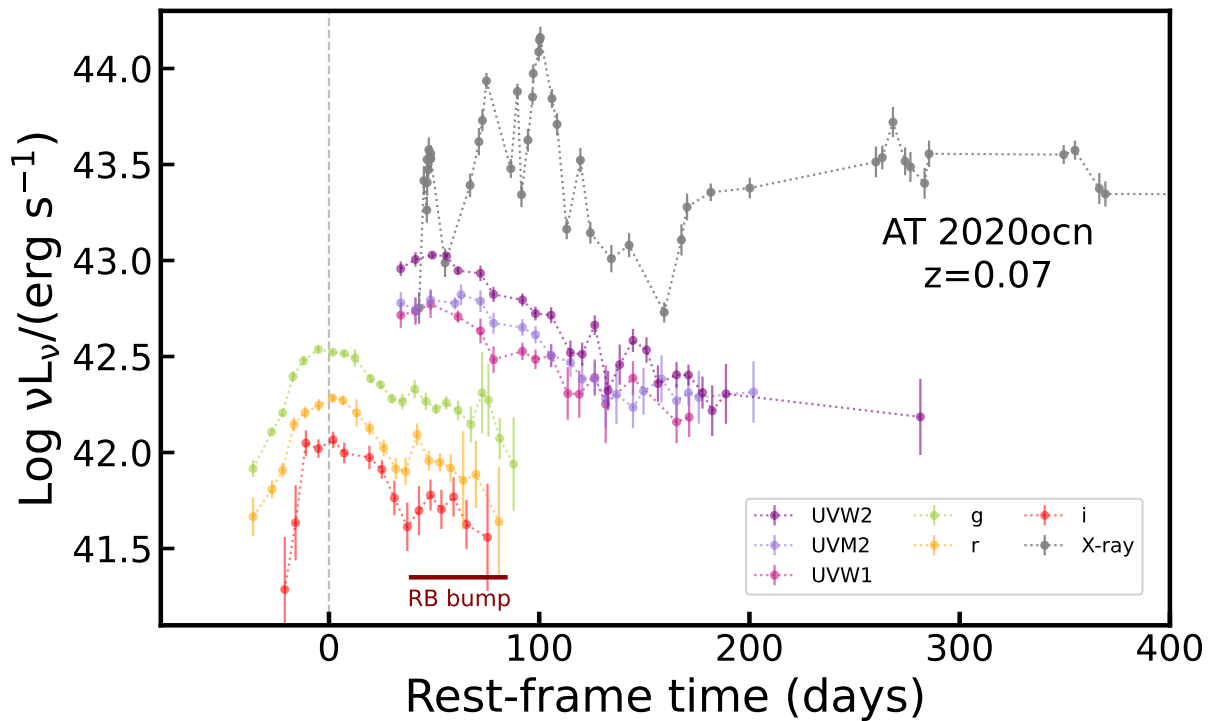


Figure S11: **Multi-band light curves of AT 2020ocn with a relatively weak RB bump.** The host subtracted light curves are obtained from ZTF sample (37). The RB bump is observed  $\sim 70$  days after light maximum, although no UV data covers the first peak. The brown line indicates the RB bump and the grey dashed line indicates the first peak light. All the light curves are binned every 5 days for clarity.

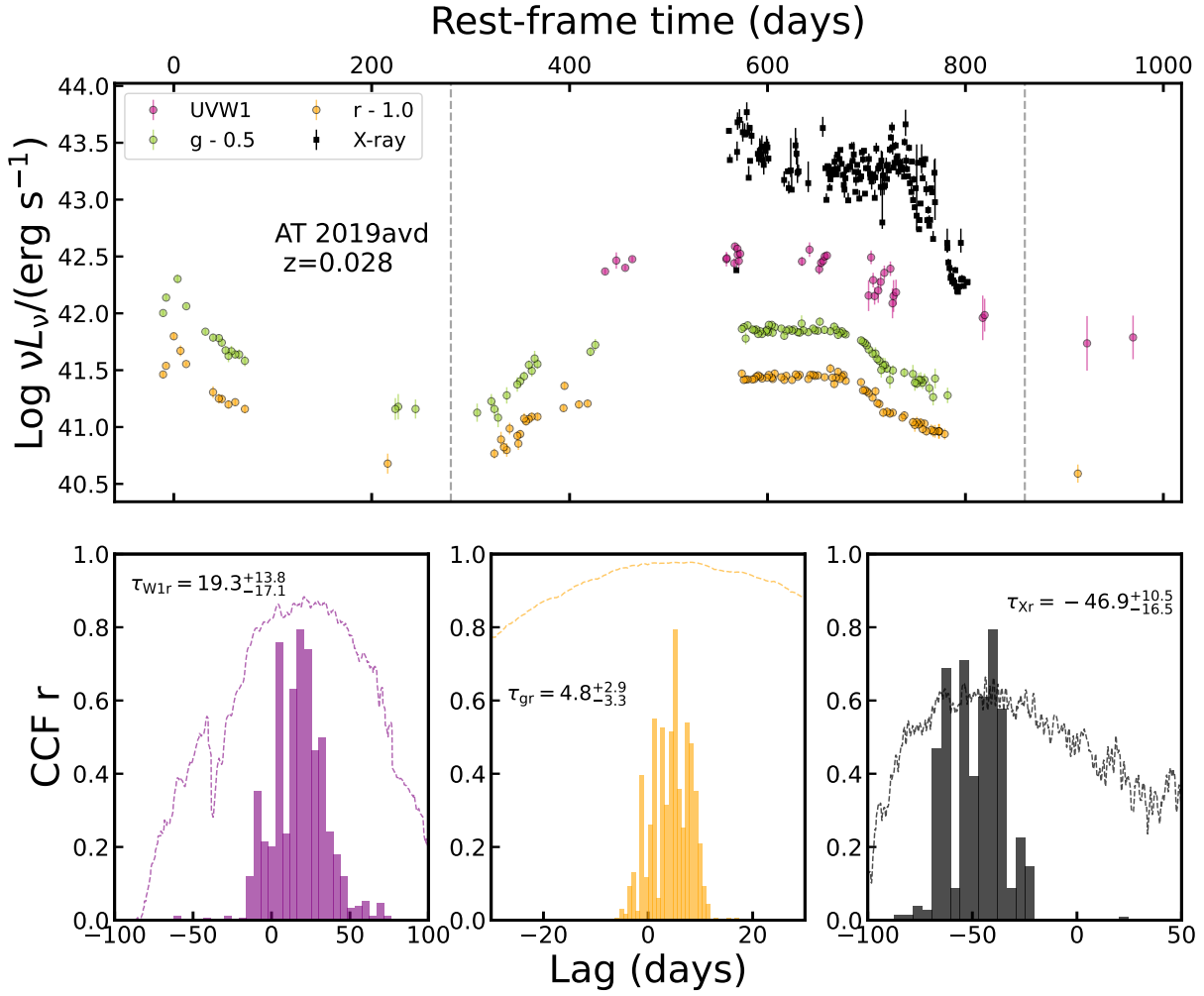


Figure S12: **Multi-band light curves and lag measurements of a TDE AT2019avd showing a broad RB bump (60, 62).** Upper panel: light curves are obtained from ZTF survey, Swift, and NICER (0.3–2 keV) telescopes (62). Grey dashed lines bracket the RB region used for lag measurement after detrending. Bottom panels: inter-band lags are measured with the ICCF method. Positive-direction lags are detected in  $W1r$  ( $1.1\sigma$ ) and  $gr$  ( $1.7\sigma$ ) bands, albeit with larger uncertainties. While a significant negative-direction lag ( $4.5\sigma$ ) is detected between soft X-ray and  $r$  band. CCF curves (dashed lines) are plotted in each panel and all the lags are in unit of days.



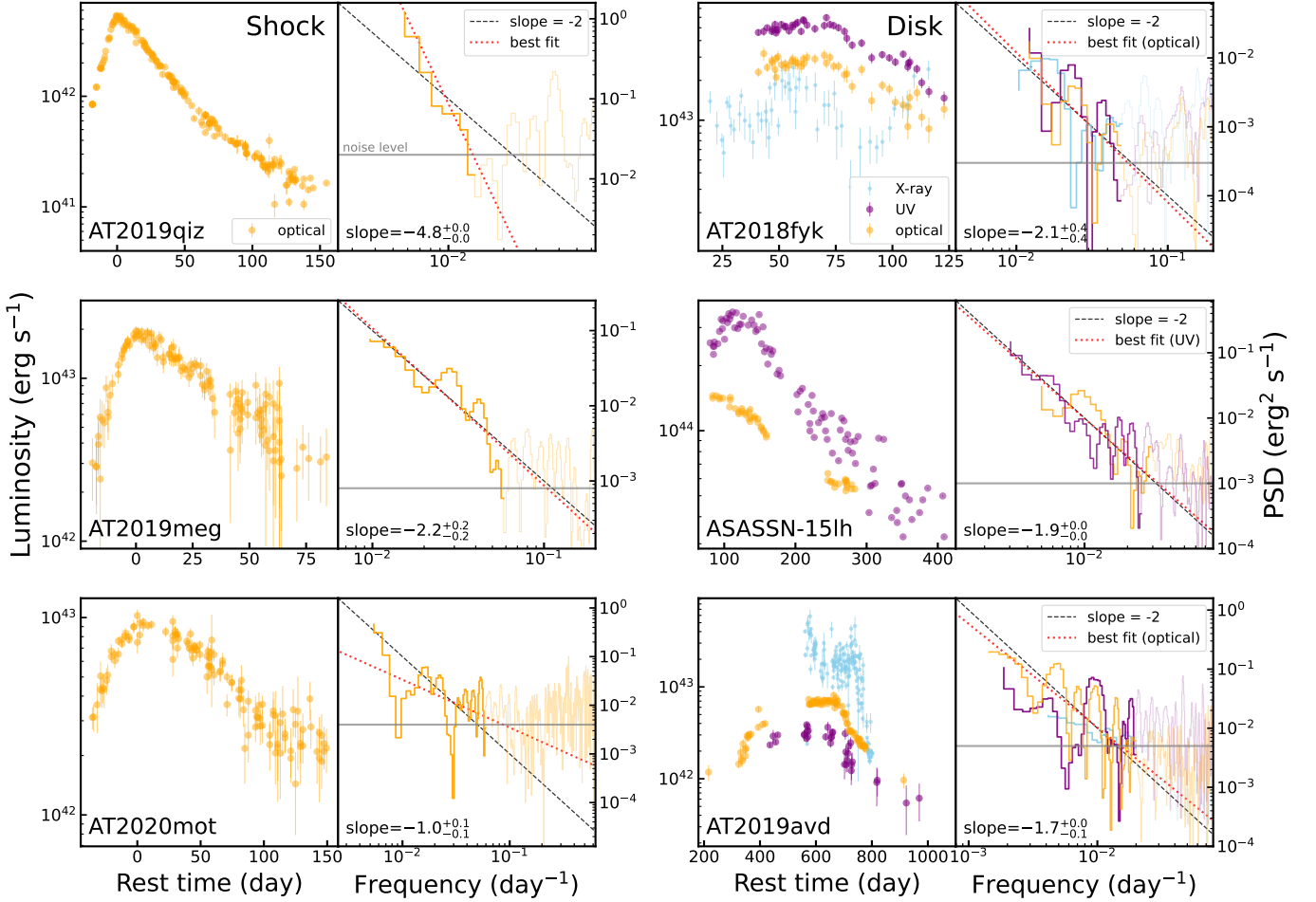


Figure S13: **Examples of light curves and PSDs from shock flare and disk RB bump.** Left panel: light curves and PSDs of shock contribution. Three TDEs are selected from the ZTF sample (37). Right panel: truncated light curves and PSDs of disk contribution. Light curves are truncated RB segments of the whole light curves of three TDEs from Figure S10. The PSDs are fitted with a single power-law ( $\text{PSD} \propto \nu^\alpha$ ) model (red dotted line) after removing the measurement noise region (transparent lines). A power-law slope of  $-2$  (black dashed line) is overplotted for comparison. Note that the PSD slope of ASASSN-15lh is obtained from the UV light curve since the optical one is significantly contaminated by shock component.

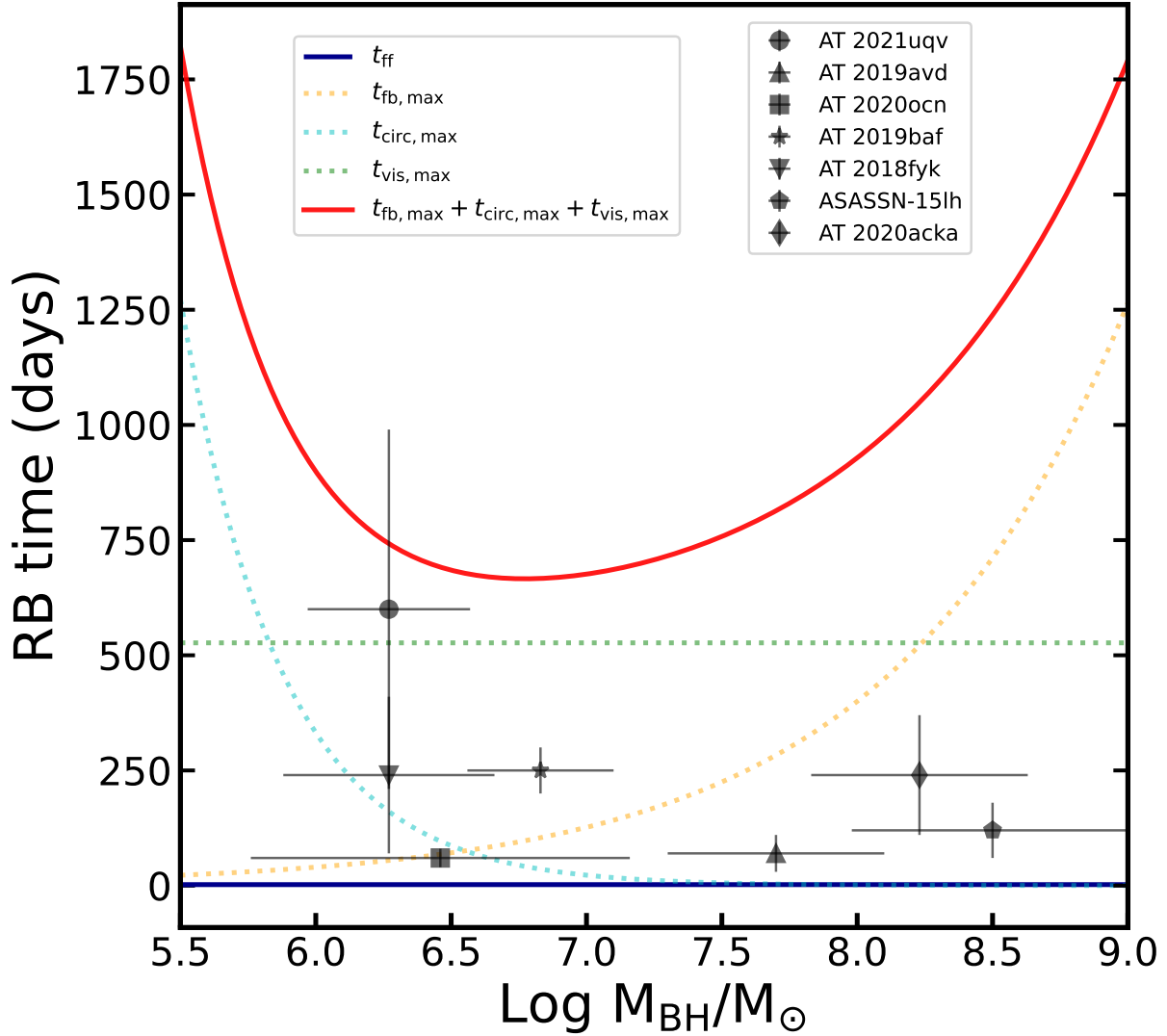


Figure S15: **BH mass vs. RB time.** Different timescales (freefall  $t_{\text{ff}}$ , maximum fallback  $t_{\text{fb,max}}$ , maximum circularization  $t_{\text{circ,max}}$ , maximum viscosity  $t_{\text{vis,max}}$ ) as a function of BH mass. The  $t_{\text{RB}}$  should be larger than  $t_{\text{ff}}$  (dark blue line) if the gas directly plunge into the BH, yet smaller than  $t_{\text{fb}} + t_{\text{circ,max}} + t_{\text{vis,max}}$  if the gas is gradually circularized and accreted into BH. The black symbols correspond to 7 TDEs with RB bumps in Figure S10 and Table S3. The uncertainty of RB time is estimated using  $0.5t_{\text{duration}}$ .

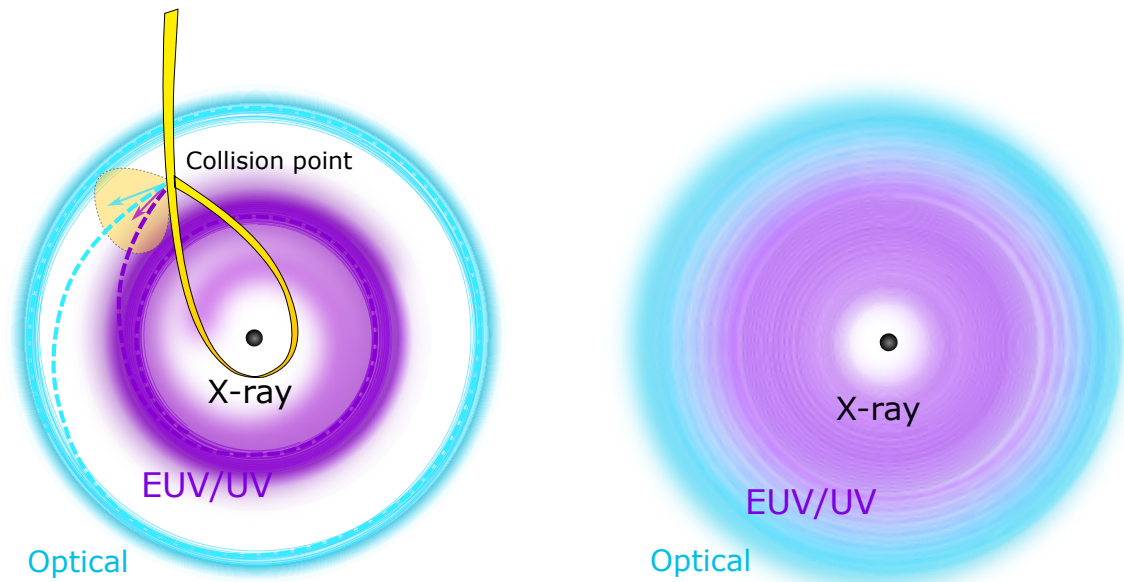


Figure S16: **A cartoon of the disk formation processing.** Left panel demonstrates two representative inflowing/outflowing gas streams with different angular momentum are circularizing to form EUV/UV and optical emitting annuli of the nascent disk. Since the gas angular momentum is continuously distributed after shock collision, the right panel shows a complete disk with the gaps are filled by spiraling or outflowing gas. The collision point is thought to be close to the UV/EUV emitting ring.

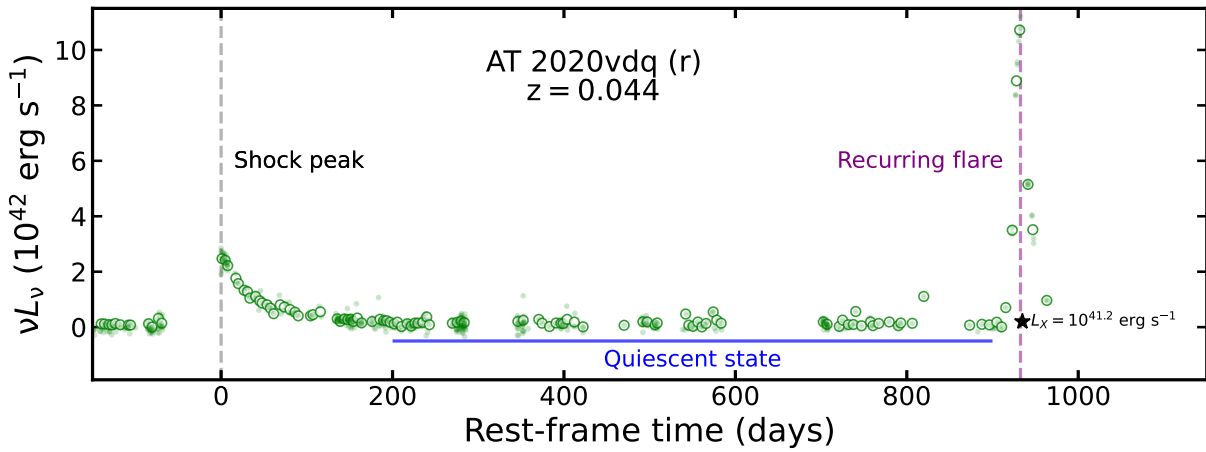


Figure S17: **A TDE of AT 2020vdq showing a recurring flare.** The ZTF-r light curves (host subtracted) are binned with a 1-day window for clarity, and the original data are also shown with the transparent green dots. Black star represents the detected X-ray luminosity from XMM-Newton telescope.

**Table S1: Combined multi-band light curves of AT 2019qiz.** Photometries observed by Swift, ZTF, LCO, and Swope telescopes are directly drawn from previous works (15, 16). To remove the systematic difference in photometry, optical light curves obtained from ref (15) are shifted by  $-0.34$ ,  $-0.26$ , and  $-0.25$   $\text{erg s}^{-1}$  in *gri* bands, respectively. The full table is available online.

MJD	$\log(\nu L_\nu/\text{erg s}^{-1})$	$\log(\nu L_{\nu,\text{err}}/\text{erg s}^{-1})$	band	telescope	Ref
58753.059	43.004	0.016	UVW2	Swift	1
58755.388	43.040	0.020	UVW2	Swift	1
58756.436	43.128	0.020	UVW2	Swift	1
58763.212	43.380	0.020	UVW2	Swift	1
58766.074	43.308	0.016	UVW2	Swift	1
58769.324	43.204	0.016	UVW2	Swift	1
58772.787	43.116	0.044	UVW2	Swift	1
58778.548	42.936	0.020	UVW2	Swift	1
58781.681	42.704	0.024	UVW2	Swift	1
58784.603	42.800	0.020	UVW2	Swift	1
⋮	⋮	⋮	⋮	⋮	⋮

**Table S2: Inter-band lags of the collision-induced flare for 18 ZTF TDEs.** Redshift and blackbody radius  $R_{\text{bb}}$  are drawn from a previous study (37). Inter-band lags are measured with ICCF method if the light curves are available.

Name	$z$	$\log R_{\text{bb}}$ (cm)	$\tau_{\text{gr}}$ (days)	$\tau_{\text{gi}}$ (days)	$\tau_{\text{M2g}}$ (days)
AT2018lni	0.14	$15.09^{+0.07}_{-0.06}$	$0.2^{+4.8}_{-4.5}$		
AT2018lna	0.09	$14.84^{+0.04}_{-0.04}$	$-0.1^{+4.0}_{-2.1}$		
AT2019cho	0.19	$15.28^{+0.05}_{-0.04}$	$-0.3^{+0.8}_{-2.7}$		
AT2019bhf	0.12	$15.13^{+0.09}_{-0.08}$	$1.1^{+3.0}_{-6.5}$	$0.6^{+7.3}_{-13.8}$	
AT2019azh	0.02	$14.98^{+0.03}_{-0.02}$	$0.5^{+1.3}_{-1.3}$		$5.4^{+5.4}_{-2.9}$
AT2019ehz	0.07	$15.03^{+0.03}_{-0.03}$	$1.0^{+0.3}_{-0.2}$	$2.0^{+1.2}_{-1.6}$	
AT2019mha	0.15	$15.05^{+0.09}_{-0.10}$	$-0.1^{+1.7}_{-1.5}$	$2.6^{+4.5}_{-3.1}$	
AT2019meg	0.15	$15.01^{+0.02}_{-0.02}$	$0.3^{+0.9}_{-1.3}$	$3.1^{+2.1}_{-2.2}$	
AT2019lwu	0.12	$15.19^{+0.06}_{-0.05}$	$0.8^{+1.4}_{-1.8}$	$3.1^{+5.3}_{-2.8}$	
AT2019qiz	0.02	$14.93^{+0.03}_{-0.03}$	$0.9^{+0.7}_{-0.7}$		$1.0^{+0.4}_{-0.2}$
AT2019teq	0.09	$14.95^{+0.03}_{-0.03}$	$0.6^{+2.4}_{-1.8}$		
AT2020pj	0.07	$15.00^{+0.04}_{-0.03}$	$3.1^{+4.0}_{-3.4}$		
AT2020opy	0.16	$15.12^{+0.02}_{-0.02}$		$2.8^{+3.2}_{-2.4}$	
AT2020mot	0.07	$15.01^{+0.03}_{-0.03}$	$1.3^{+2.7}_{-2.5}$		
AT2020mbq	0.09	$15.07^{+0.05}_{-0.04}$	$0.4^{+1.5}_{-1.0}$		
AT2020riz	0.43	$15.40^{+0.10}_{-0.10}$	$-0.1^{+1.6}_{-1.3}$		
AT2020wey	0.03	$14.50^{+0.04}_{-0.04}$	$1.0^{+0.6}_{-0.5}$		
AT2020zso	0.06	$14.99^{+0.02}_{-0.02}$	$-0.0^{+0.6}_{-0.8}$		$4.1^{+1.2}_{-1.8}$

**Table S3: Properties of 7 TDEs with RB bump.** Redshift and BH mass are drawn from previous works listed in the last column.  $t_{\text{start}}$  is the start point of the RB bump, defined as the lowest point between the first and second peaks in Figure S10.  $t_{\text{peak}}$  is defined as the highest point on the RB bump.  $t_{\text{duration}}$  is the duration time of RB bump, roughly estimated based on the convex region, although light curves are not complete. We found no potential correlations between black mass and different timescales.

Name	$z$	$t_{\text{start}}$ days	$t_{\text{peak}}$ days	$t_{\text{duration}}$ days	Log $M_{\text{BH}}/M_{\odot}$	BH method	Ref
BH mass $\leq 10^8 M_{\odot}$ :							
AT 2021uqv	0.106	70	240	270	$6.3^{+0.4}_{-0.4}$	$M_{\text{BH}} - \sigma_*$	(38)
AT 2019avd	0.028	210	600	600	$6.3^{+0.3}_{-0.3}$	single-epoch spec.	(60, 62)
AT 2020ocn	0.070	40	60	50	$6.5^{+0.7}_{-0.7}$	$M_{\text{BH}} - \sigma_*$	(82)
AT 2019baf	0.089	200	250	150	$6.8^{+0.3}_{-0.3}$	$M_{\text{BH}} - M_{\text{gal}}$	(38)
AT 2018fyk	0.059	30	70	550	$7.7^{+0.4}_{-0.4}$	$M_{\text{BH}} - \sigma_*$	(43)
BH mass $> 10^8 M_{\odot}$ :							
AT 2020acka	0.338	80	210	600	$8.2^{+0.4}_{-0.4}$	$M_{\text{BH}} - \sigma_*$	(38)
ASASSN-15lh	0.233	60	120	>300	$8.5^{+0.5}_{-0.5}$	$M_{\text{BH}} - L$	(26)

**Table S4: Priors for light-curve detrending using MCMC analysis.**

Parameter	Description	Prior
$\log L_{\text{peak}}$	Peak luminosity	$[\log (L_{\text{max}}/2), \log (2L_{\text{max}})]$
$t_{\text{peak}}$	Peak time	$[-5, 5]$ days
$t_0$	Power-law normalization	$[0, 3]$ days
$p$	Power-law index	$[-5, 0]$
$\log \tau$	Exponential decay time	$[0, 3]$ days



**Table S5: Light curve detrending properties for 7 additional TDEs with RB bumps.** Note that  $p$  and  $\log \tau$  describe the decay speed of the light curves in the power-law or exponential modeling.

Name	band	$\log L_{\text{peak}}$	$t_{\text{peak}}$	$p / \log \tau$	$\log t_0$	$\chi^2_{\nu}$
AT2021uqv (PL)	g	$43.28^{+0.06}_{-0.05}$	$-0.28^{+3.71}_{-3.36}$	$-1.08^{+0.20}_{-0.39}$	$1.49^{+0.21}_{-0.18}$	1.79
	r	$43.06^{+0.04}_{-0.04}$	$-0.43^{+3.69}_{-3.24}$	$-1.50^{+0.42}_{-0.77}$	$1.76^{+0.24}_{-0.23}$	2.32
AT2019baf (PL)	g	$43.54^{+0.04}_{-0.04}$	$0.10^{+3.36}_{-3.42}$	$-3.68^{+0.30}_{-0.33}$	$2.16^{+0.06}_{-0.06}$	1.42
	r	$43.48^{+0.05}_{-0.05}$	$-0.10^{+3.45}_{-3.40}$	$-2.98^{+0.23}_{-0.27}$	$1.94^{+0.06}_{-0.06}$	1.92
	i	$43.46^{+0.28}_{-0.15}$	$0.04^{+3.28}_{-3.59}$	$-2.10^{+0.56}_{-1.07}$	$1.66^{+0.36}_{-0.45}$	1.1
AT2019avd (PL)	g	$43.26^{+0.24}_{-0.15}$	$-1.76^{+3.35}_{-2.28}$	$-0.83^{+0.09}_{-0.11}$	$0.83^{+0.27}_{-0.41}$	0.58
	r	$43.13^{+0.15}_{-0.08}$	$0.05^{+4.42}_{-3.56}$	$-1.01^{+0.29}_{-0.46}$	$1.40^{+0.32}_{-0.49}$	0.77
AT2018fyk (Exp.)	UVW2	$44.29^{+0.09}_{-0.09}$	$4.85^{+6.63}_{-6.66}$	$1.51^{+0.02}_{-0.02}$		1.92
	UVM2	$44.12^{+0.07}_{-0.07}$	$4.71^{+6.69}_{-6.61}$	$1.60^{+0.03}_{-0.03}$		1.73
	UVW1	$44.04^{+0.08}_{-0.08}$	$4.83^{+6.63}_{-6.62}$	$1.58^{+0.03}_{-0.03}$		0.96
	U	$43.78^{+0.09}_{-0.08}$	$4.81^{+6.60}_{-6.67}$	$1.53^{+0.04}_{-0.04}$		1.40
ASASSN-15lh (Exp.)	UVW2	$45.83^{+0.03}_{-0.02}$	$1.92^{+1.87}_{-1.70}$	$2.97^{+0.02}_{-0.04}$		2.23
	UVM2	$44.12^{+0.07}_{-0.07}$	$4.71^{+6.69}_{-6.61}$	$1.60^{+0.03}_{-0.03}$		1.73
	UVW1	$44.04^{+0.08}_{-0.08}$	$4.83^{+6.63}_{-6.62}$	$1.58^{+0.03}_{-0.03}$		0.96
	U	$43.78^{+0.09}_{-0.08}$	$4.81^{+6.60}_{-6.67}$	$1.53^{+0.04}_{-0.04}$		1.40
	B	$45.04^{+0.03}_{-0.04}$	$-0.19^{+3.55}_{-3.32}$	$1.65^{+0.02}_{-0.02}$		1.39
	g	$44.95^{+0.04}_{-0.04}$	$-0.05^{+3.49}_{-3.45}$	$1.66^{+0.04}_{-0.04}$		0.10
	V	$44.85^{+0.03}_{-0.03}$	$-0.04^{+3.40}_{-3.38}$	$1.68^{+0.02}_{-0.02}$		1.06
	r	$44.62^{+0.04}_{-0.03}$	$-0.16^{+3.54}_{-3.29}$	$1.76^{+0.06}_{-0.05}$		0.18
	i	$44.32^{+0.03}_{-0.03}$	$-0.26^{+3.49}_{-3.29}$	$1.88^{+0.07}_{-0.06}$		0.41
AT2020acka (Exp.)	g	$44.77^{+0.03}_{-0.04}$	$-0.08^{+3.45}_{-3.29}$	$1.63^{+0.01}_{-0.01}$		4.06
	r	$44.45^{+0.03}_{-0.03}$	$-0.10^{+3.44}_{-3.40}$	$1.70^{+0.01}_{-0.01}$		2.53
	i	$44.22^{+0.03}_{-0.03}$	$-0.14^{+3.56}_{-3.39}$	$1.70^{+0.03}_{-0.03}$		1.28
AT2020ocn (Exp.)	g	$42.56^{+0.02}_{-0.02}$	$-1.63^{+2.30}_{-2.29}$	$1.72^{+0.04}_{-0.04}$		1.33
	r	$42.33^{+0.03}_{-0.03}$	$-1.62^{+2.24}_{-2.27}$	$1.60^{+0.05}_{-0.04}$		0.91
	i	$42.09^{+0.05}_{-0.04}$	$-1.46^{+2.34}_{-2.41}$	$1.74^{+0.14}_{-0.11}$		1.53

**Table S6: Lag measurements of the RB bump in four TDEs.** Note that stage A of AT 2018fyk is on the RB bump, while stage B is after the RB bump. Empty cell indicates no lag is detectable, e.g., low light-curve cadence, no significant variabilities, or too large lag uncertainties.

Name	Log $M_{\text{BH}}/M_{\odot}$	X-ray vs. UV (day)	X-ray vs. Opt (day)	UV vs. Opt (day)	Opt- $g$ vs. Opt- $r$ (day)
ASASSN-15lh	$8.5 \pm 0.5$			$15.0^{+3.8}_{-3.3}$	
AT 2019avd	$6.3 \pm 0.3$	$-55.2^{+68.6}_{-28.9}$	$-46.9^{+10.5}_{-16.5}$	$19.3^{+13.8}_{-17.1}$	$4.8^{+2.9}_{-3.3}$
AT 2020ocn	$6.5 \pm 0.7$	$-42^{+12.1}_{-3.4}$	$-42^{+12.1}_{-3.4}$		
AT 2018fyk (A)	$7.7 \pm 0.4$	$9.2^{+6.1}_{-6.0}$			
AT 2018fyk (B)	$7.7 \pm 0.4$	$-4.0^{+1.4}_{-1.4}$			

## Acknowledgments

HXG and SLL thank Fukun Liu, Kirk Krista, Weimin Gu, Guobin Mou for useful discussions. **Funding:** HXG acknowledges support from the National Key R&D Program of China No. 2022YFF0503402. SLL is supported by the National Natural Science Foundation of China (No. 12273089). DFB is supported by the NSFC (No. 12173065). The Center for Computational Astrophysics at the Flatiron Institute is supported by the Simons Foundation. TGW is supported by the National Natural Science Foundation of China (No. 11833007) and the China Manned Space Project (CMS-CSST-2021-A12). YNW is supported by the Strategic Priority Research Program of the Chinese Academy of Sciences (No. XDB0550200). MYS acknowledges support from the NSFC (No. 12322303) and the Natural Science Foundation of Fujian Province of China (No. 2022J06002). MFG is supported by the Shanghai Pilot Program for Basic Research-Chinese Academy of Science, Shanghai Branch (JCYJ-SHFY-2021-013), the National SKA Program of China (Grant No. 2022SKA0120102), the science research grants from the China Manned Space Project with No. CMSCSST-2021-A06, and the Original Innovation Program of the Chinese Academy of Sciences (E085021002). **Author contributions:** HXG conceived this project. HXG and JBS led the data analysis and the manuscript writing; YFJ and SLL led the theoretical interpretation and co-wrote the manuscript; HXG, TGW, SLL, and YFJ established the unified TDE picture; All authors contributed to the results and commented on the manuscript. **Competing interests:** The authors declare that they have no competing interests. **Data and materials availability:** ZTF and Swift light curves are available through their separate public data archives. Light curves of individual TDE are all available at corresponding literature. Combined light curves of AT 2019qiz are listed in Table S1. **Code availability:** The PyCCF code for lag measurement is publicly available at <https://ui.adsabs.harvard.edu/abs/2018ascl>.

soft05032S/abstract. The emcee package for affine invariant MCMC Ensemble sampler is publicly available at <https://emcee.readthedocs.io/en/stable/>.

## References and Notes

1. M. J. Rees, *Nat.* **333**, 523 (1988).
2. C. R. Evans, C. S. Kochanek, *Astrophys. J.* **346**, L13 (1989).
3. T. Piran, G. Svirski, J. Krolik, R. M. Cheng, H. Shiokawa, *Astrophys. J.* **806**, 164 (2015).
4. A. Loeb, A. Ulmer, *Astrophys. J.* **489**, 573 (1997).
5. B. D. Metzger, N. C. Stone, *Mon. Not. R. Astron. Soc.* **461**, 948 (2016).
6. E. S. Phinney, *The Center of the Galaxy*, M. Morris, ed. (1989), vol. 136, p. 543.
7. C. S. Kochanek, *et al.*, *P. Astron. Soc. Pac.* **129**, 104502 (2017).
8. E. C. Bellm, *et al.*, *P. Astron. Soc. Pac.* **131**, 018002 (2019).
9. S. Gezari, *Annu. Rev. Astron. Astrophys.* **59**, 21 (2021).
10. C. Bonnerot, N. C. Stone, *Scientific Studies of Reading* **217**, 16 (2021).
11. D. R. Pasham, *et al.*, *Astrophys. J.* **837**, L30 (2017).
12. N. Roth, D. Kasen, J. Guillochon, E. Ramirez-Ruiz, *Astrophys. J.* **827**, 3 (2016).
13. L. Dai, J. C. McKinney, N. Roth, E. Ramirez-Ruiz, M. C. Miller, *Astrophys. J.* **859**, L20 (2018).
14. M. A. Abramowicz, B. Czerny, J. P. Lasota, E. Szuszkiewicz, *Astrophys. J.* **332**, 646 (1988).

15. M. Nicholl, *et al.*, *Mon. Not. R. Astron. Soc.* **499**, 482 (2020).
16. T. Hung, *et al.*, *Astrophys. J.* **917**, 9 (2021).
17. I. M. McHardy, *et al.*, *Mon. Not. R. Astron. Soc.* **444**, 1469 (2014).
18. M. M. Fausnaugh, *et al.*, *Astrophys. J.* **821**, 56 (2016).
19. E. M. Cackett, M. C. Bentz, E. Kara, *iScience* **24**, 102557 (2021).
20. P. Arévalo, I. Papadakis, B. Kuhlbrodt, W. Brinkmann, *Astron. Astrophys.* **430**, 435 (2005).
21. M. Pahari, *et al.*, *Mon. Not. R. Astron. Soc.* **494**, 4057 (2020).
22. C. Bonnerot, E. M. Rossi, G. Lodato, *Mon. Not. R. Astron. Soc.* **464**, 2816 (2017).
23. W. Lu, C. Bonnerot, *Mon. Not. R. Astron. Soc.* **492**, 686 (2020).
24. Z. L. Andalman, M. T. P. Liska, A. Tchekhovskoy, E. R. Coughlin, N. Stone, *Mon. Not. R. Astron. Soc.* **510**, 1627 (2022).
25. E. Steinberg, N. C. Stone, *arXiv e-prints* p. arXiv:2206.10641 (2022).
26. G. Leloudas, *et al.*, *Nature Astronomy* **1**, 0002 (2016).
27. S. Dong, *et al.*, *Science* **351**, 257 (2016).
28. R. Margutti, *et al.*, *Astrophys. J.* **836**, 25 (2017).
29. A. P. Lobban, *et al.*, *Mon. Not. R. Astron. Soc.* **494**, 1165 (2020).
30. J. V. Hernández Santisteban, *et al.*, *Mon. Not. R. Astron. Soc.* **498**, 5399 (2020).
31. E. M. Cackett, *et al.*, *Astrophys. J.* **857**, 53 (2018).

32. F. M. Vincentelli, *et al.*, *Mon. Not. R. Astron. Soc.* **504**, 4337 (2021).
33. E. Kara, *et al.*, *Astrophys. J.* **922**, 151 (2021).
34. R. Edelson, *et al.*, *Astrophys. J.* **840**, 41 (2017).
35. A. Mummery, S. A. Balbus, *Mon. Not. R. Astron. Soc.* **497**, L13 (2020).
36. X.-L. Liu, L.-M. Dou, J.-H. Chen, R.-F. Shen, *Astrophys. J.* **925**, 67 (2022).
37. E. Hammerstein, *et al.*, *Astrophys. J.* **942**, 9 (2023).
38. Y. Yao, *et al.*, *Astrophys. J.* **955**, L6 (2023).
39. T. Wevers, *et al.*, *Mon. Not. R. Astron. Soc.* **488**, 4816 (2019).
40. T. Wevers, *Mon. Not. R. Astron. Soc.* **497**, L1 (2020).
41. T. Wevers, *et al.*, *Astrophys. J.* **912**, 151 (2021).
42. T. W. S. Holoien, *et al.*, *Mon. Not. R. Astron. Soc.* **463**, 3813 (2016).
43. T. Wevers, *et al.*, *Astrophys. J.* **942**, L33 (2023).
44. J. J. Somalwar, *et al.*, *arXiv e-prints* p. arXiv:2310.03782 (2023).
45. Y.-F. Jiang, J. Guillochon, A. Loeb, *Astrophys. J.* **830**, 125 (2016).
46. X. Huang, S. W. Davis, Y.-f. Jiang, *Astrophys. J.* **953**, 117 (2023).
47. S. van Velzen, *et al.*, *Astrophys. J.* **872**, 198 (2019).
48. P. G. Jonker, N. C. Stone, A. Generozov, S. van Velzen, B. Metzger, *Astrophys. J.* **889**, 166 (2020).

49. Lu, W. & Kumar, P. 2018, *Astrophys. J.*, 865, 128. doi:10.3847/1538-4357/aad54a
50. B. M. Peterson, *et al.*, *P. Astron. Soc. Pac.* **110**, 660 (1998).
51. M. Sun, C. J. Grier, B. M. Peterson, PyCCF: Python Cross Correlation Function for reverberation mapping studies, Astrophysics Source Code Library, record ascl:1805.032 (2018).
52. R. J. White, B. M. Peterson, *P. Astron. Soc. Pac.* **106**, 879 (1994).
53. B. Paczynski, *Astrophys. J.* **267**, 315 (1983).
54. N. I. Shakura, R. A. Sunyaev, *Astron. Astrophys.* **24**, 337 (1973).
55. H. Guo, A. J. Barth, S. Wang, *Astrophys. J.* **940**, 20 (2022).
56. R. Edelson, *et al.*, *Astrophys. J.* **870**, 123 (2019).
57. W. F. Welsh, *P. Astron. Soc. Pac.* **111**, 1347 (1999).
58. S. van Velzen, *et al.*, *Astrophys. J.* **908**, 4 (2021).
59. D. Foreman-Mackey, D. W. Hogg, D. Lang, J. Goodman, *P. Astron. Soc. Pac.* **125**, 306 (2013).
60. A. Malyali, *et al.*, *Astron. Astrophys.* **647**, A9 (2021).
61. J.-H. Chen, L.-M. Dou, R.-F. Shen, *Astrophys. J.* **928**, 63 (2022).
62. Y. Wang, *et al.*, *Mon. Not. R. Astron. Soc.* **520**, 2417 (2023).
63. N. R. Lomb, *Astrophysics and Space Science* **39**, 447 (1976).
64. B. C. Kelly, J. Bechtold, A. Siemiginowska, *Astrophys. J.* **698**, 895 (2009).
65. C. L. MacLeod, *et al.*, *Astrophys. J.* **721**, 1014 (2010).

66. Y. Zu, C. S. Kochanek, B. M. Peterson, *Astrophys. J.* **735**, 80 (2011).
67. P. Uttley, E. M. Cackett, A. C. Fabian, E. Kara, D. R. Wilkins, *The Astronomy and Astrophysics Review* **22**, 72 (2014).
68. L. E. Strubbe, E. Quataert, *Mon. Not. R. Astron. Soc.* **400**, 2070 (2009).
69. J. Huang, *et al.*, *Astrophys. J.* **945**, 57 (2023).
70. R. Edelson, *et al.*, *Astrophys. J.* **806**, 129 (2015).
71. A. Koratkar, O. Blaes, *P. Astron. Soc. Pac.* **111**, 1 (1999).
72. S. W. Davis, A. Tchekhovskoy, *Annu. Rev. Astron. Astrophys.* **58**, 407 (2020).
73. J. Guillochon, M. McCourt, *Astrophys. J.* **834**, L19 (2017).
74. C. Bonnerot, D. J. Price, G. Lodato, E. M. Rossi, *Mon. Not. R. Astron. Soc.* **469**, 4879 (2017).
75. M. C. Begelman, J. Silk, *Mon. Not. R. Astron. Soc.* **464**, 2311 (2017).
76. J. Dexter, M. C. Begelman, *Mon. Not. R. Astron. Soc.* **483**, L17 (2019).
77. M. C. Begelman, P. J. Armitage, *Mon. Not. R. Astron. Soc.* **521**, 5952 (2023).
78. Y.-F. Jiang, O. Blaes, J. M. Stone, S. W. Davis, *Astrophys. J.* **885**, 144 (2019).
79. B. Mishra, *et al.*, *Astrophys. J.* **939**, 31 (2022).
80. R.-F. Shen, C. D. Matzner, *Astrophys. J.* **784**, 87 (2014).
81. M. Newsome, *et al.*, *Transient Name Server Classification Report* **2023-1865**, 1 (2023).
82. E. Hammerstein, *et al.*, *Astrophys. J.* **957**, 86 (2023).